DNA-TR-88-112

MODELS OF THE ANEURYSM IN EXPANDING LASER-PLASMA

R. E. Peterkin, Jr.
R. F. Stellingwerf
Mission Research Corporation
Plasma Sciences Division
1720 Randolph Road, SE
Albuquerque, NM 87106-4245

31 July 1988

Technical Report

CONTRACT No. DNA 001-85-C-0069

THIS WORK WAS SPONSORED BY THE DEFENSE NUCLEAR AGENCY
UNDER RDT&E RMC CODE B3220854662 RB RC 00135 25904D.

Prepared for
Director
DEFENSE NUCLEAR AGENCY
Washington, DC 20305-1000

Destroy this report when it is no longer needed. Do not return to sender.

PLEASE NOTIFY THE DEFENSE NUCLEAR AGENCY ATTN: TITL, WASHINGTON, DC 20305 1000, IF YOUR ADDRESS IS INCORRECT, IF YOU WISH IT DELETED FROM THE DISTRIBUTION LIST, OR IF THE ADDRESSEE IS NO LONGER EMPLOYED BY YOUR ORGANIZATION.

UNCLASSIFIED
SECURITY CLASSIFICATION OF THIS PAGE

AD-A200 754

REPORT DOCUMENTATION PAGE

1a. REPORT SECURITY CLASSIFICATION UNCLASSIFIED	1b. RESTRICTIVE MARKINGS
2a. SECURITY CLASSIFICATION AUTHORITY N/A since Unclassified	3. DISTRIBUTION/AVAILABILITY OF REPORT Approved for public release; distribution is unlimited.
2b. DECLASSIFICATION/DOWNGRADING SCHEDULE N/A since Unclassified	
4. PERFORMING ORGANIZATION REPORT NUMBER(S) MRC/ABQ-R-1031	5. MONITORING ORGANIZATION REPORT NUMBER(S) DNA-TR-88-112
6a. NAME OF PERFORMING ORGANIZATION Mission Research Corporation Plasma Sciences Division 6b. OFFICE SYMBOL (If applicable)	7a. NAME OF MONITORING ORGANIZATION Director Defense Nuclear Agency
6c. ADDRESS (City, State, and ZIP Code) 1720 Randolph Road, SE Albuquerque, NM 87106-4245	7b. ADDRESS (City, State, and ZIP Code) Washington, DC 20305-1000
8a. NAME OF FUNDING/SPONSORING ORGANIZATION 8b. OFFICE SYMBOL (If applicable) RAAE/Wittwer	9. PROCUREMENT INSTRUMENT IDENTIFICATION NUMBER DNA 001-85-C-0069
8c. ADDRESS (City, State, and ZIP Code)	10. SOURCE OF FUNDING NUMBERS PROGRAM ELEMENT NO. 62715H; PROJECT NO RB; TASK NO RC; WORK UNIT ACCESSION NO DH008713

11. TITLE (Include Security Classification)
MODELS OF THE ANEURYSM IN EXPANDING LASER-PLASMA

12. PERSONAL AUTHOR(S)
Peterkin, Robert E., Jr.; Stellingwerf, Robert F.

13a. TYPE OF REPORT	13b. TIME COVERED	14. DATE OF REPORT (Year, Month, Day)	15. PAGE COUNT
Technical	FROM 850502 TO 880731	880731	96

16. SUPPLEMENTARY NOTATION
This work was sponsored by the Defense Nuclear Agency under RDT&E RMC Code B322085 4662 RB RC 00135 25904D.

17 COSATI CODES			18. SUBJECT TERMS (Continue on reverse if necessary and identify by block number)
FIELD	GROUP	SUB-GROUP	Laser Plasma; Plasma Physics; Laser Aneurysm; Blast Wave; Laser Experiment; Plasma Instabilities
9	3		
20	9		

19. ABSTRACT (Continue on reverse if necessary and identify by block number)

This report describes theoretical models of laser-plasma experiments currently under way at the Naval Research Laboratory (NRL) in which hot laser-irradiated target debris expands into a few Torr background gas. The most interesting characteristics of these experiments are the formation and evolution of a spherical blast wave, and in some cases, the appearance of one or more distinctive protuberances or "aneurysms" on the expanding wave. Many possible mechanisms for the formation of these structures have been suggested, ranging from instabilities in the blast wave itself to the effects of jets of material ejected from the target. Many of these mechanisms are of interest to the problem of early-time structuring in high altitude nuclear bursts. In this report we discuss a series of magnetohydrodynamic models that accurately describe this phenomenon, and identify the processes that mold the blast wave and the aneurysm. We show that in most cases the aneurysm can be explained by a channel heating mechanism due to inverse bremsstrahlung absorption in the laser channel. A simple model is derived that clearly

20. DISTRIBUTION/AVAILABILITY OF ABSTRACT ☐ UNCLASSIFIED/UNLIMITED ☒ SAME AS RPT ☐ DTIC USERS	21. ABSTRACT SECURITY CLASSIFICATION UNCLASSIFIED
22a. NAME OF RESPONSIBLE INDIVIDUAL Sandra E. Young	22b. TELEPHONE (Include Area Code) (202) 325-7042 22c. OFFICE SYMBOL DNA/CSTI

DD FORM 1473, 84 MAR — 83 APR edition may be used until exhausted. All other editions are obsolete.

SECURITY CLASSIFICATION OF THIS PAGE
UNCLASSIFIED

19. ABSTRACT (Continued)

shows this effect and matches the detailed two-dimensional models as well as the experimental results. The effects of laser-target interaction, thermal conduction, radiation cooling, multiple materials, self-generated magnetic fields, and ambient magnetic fields are included and discussed.

PREFACE

We have benefited from many fruitful discussions with M. H. Frese and J. Ruff of MRC, and with the Naval Research Laboratory (NRL) experimentalists, especially B. H. Ripin and J. A. Stamper (who kindly provided us with the shadowgraphs).

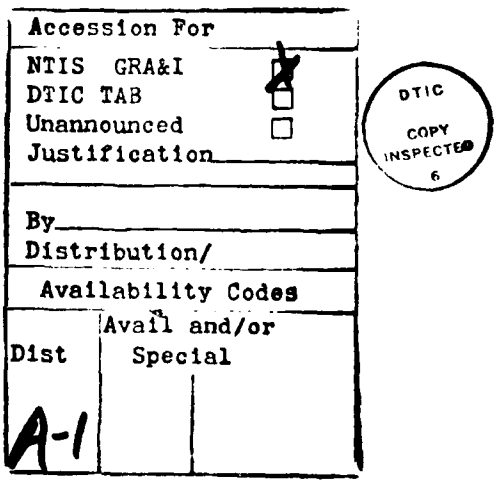

CONVERSION TABLE

Conversion factors for U.S. Customary to metric (SI) units of measurement

MULTIPLY TO GET	BY	TO GET DIVIDE
angstrom	1.000 000 X E -10	meters (m)
atmosphere (normal)	1.013 25 X E +2	kilo pascal (kPa)
bar	1.000 000 X E +2	kilo pascal (kPa)
barn	1.000 000 X E -28	meter^2 (m^2)
British thermal unit (thermochemical)	1.054 350 X E +3	joule (J)
calorie (thermochemical)	4.184 000	joule (J)
cal (thermochemical)/cm^2	4.184 000 X E -2	mega joule/m^2 (MJ/m^2)
curie	3.700 000 X E +1	*giga becquerel (GBq)
degree (angle)	1.745 329 X E -2	radian (rad)
degree Fahrenheit	$t_K = (t°F + 459.67)/1.8$	degree kelvin (K)
electron volt	1.602 19 X E -19	joule (J)
erg	1.000 000 X E -7	joule (J)
erg/second	1.000 000 X E -7	watt (W)
foot	3.048 000 X E -1	meter (m)
foot-pound-force	1.355 818	joule (J)
gallon (U.S. liquid)	3.785 412 X E -3	meter^3 (m^3)
inch	2.540 000 X E -2	meter (m)
jerk	1.000 000 X E +9	joule (J)
joule/kilogram (J/kg) (radiation dose absorbed)	1.000 000	Gray (Gy)
kilotons	4.183	terajoules
kip (1000 lbf)	4.448 222 X E +3	newton (N)
kip/inch^2 (ksi)	6.894 757 X E +3	kilo pascal (kPa)
klap	1.000 000 X E +2	newton-second/m^2 (N-s/m^2)
micron	1.000 000 X E -6	meter (m)
mil	2.540 000 X E -5	meter (m)
mile (international)	1.609 344 X E +3	meter (m)
ounce	2.834 952 X E -2	kilogram (kg)
pound-force (lbs avoirdupois)	4.448 222	newton (N)
pound-force inch	1.129 848 X E -1	newton-meter (N·m)
pound-force/inch	1.751 268 X E +2	newton/meter (N/m)
pound-force/foot^2	4.788 026 X E -2	kilo pascal (kPa)
pound-force/inch^2 (psi)	6.894 757	kilo pascal (kPa)
pound-mass (lbm avoirdupois)	4.535 924 X E -1	kilogram (kg)
pound-mass-foot^2 (moment of inertia)	4.214 011 X E -2	kilogram-meter^2 (kg·m^2)
pound-mass/foot^3	1.601 846 X E +1	kilogram/meter^3 (kg/m^3)
rad (radiation dose absorbed)	1.000 000 X E -2	**Gray (Gy)
roentgen	2.579 760 X E -4	coulomb/kilogram (C/kg)
shake	1.000 000 X E -8	second (s)
slug	1.459 390 X E +1	kilogram (kg)
torr (mm Hg, 0° C)	1.333 22 X E -1	kilo pascal (kPa)

*The becquerel (Bq) is the SI unit of radioactivity; 1 Bq = 1 event/s.
**The Gray (Gy) is the SI unit of absorbed radiation.

TABLE OF CONTENTS

LIST OF ILLUSTRATIONS

LIST OF ILLUSTRATIONS (Continued)

LIST OF ILLUSTRATIONS (Continued)

LIST OF ILLUSTRATIONS (Continued)

SECTION 1

INTRODUCTION

From 1983 through the present, the NRL laser group has performed a large number of experiments that are of interest to the HANE community with the Pharos II and Pharos III Nd-laser and target facilities. The maximum laser energy for the earlier Pharos II experiments was on the order of 100 J, whereas the energy in experiments of interest to us with the new Pharos III facility ranged from 5 to 300 J in each of up to three beams. In most of these experiments, a single beam from the Nd-glass laser λ = 1.054 μm, τ_{fwhm} ~4 ns) is focused onto a solid planar aluminum or polystyrene (CH) target that is immersed in an ambient medium (such as nitrogen) at a pressure of between a few mTorr and 10 Torr. The laser focal spot diameter is typically between 0.2 and 1.0 mm, and the targets are thin, usually between 4 and 25 μm thick. In the subset of those experiments designated as being in the "collisional" or "high-pressure" regime, the ambient pressure is above 1 Torr. The laser, with irradiance between 10^{12} and 10^{14} Watt/cm^2, ablates target material and imparts to the ions a controllable velocity distribution ($0.1 < \Delta u/u < 1.0$) around a peak of a few 10^7 cm/sec (Grun, Stellingwerf, and Ripin, 1986, Ref. 1). In the "high-pressure" regime, expanding target plasma couples to the ambient material so that, on time scales long compared to the laser pulse length, a thin, almost spherical blast front is observed (Ripin, et al., 1986, Ref. ?). Because the debris expands in the direction of the laser beam, the blast front is not centered about the target but rather expands preferentially toward the source of the laser light.

A complete tabulation of the NRL laser shots through early 1986 is available in Reference 3 (Stellingwerf, 1987), including all shot parameters and blast wave configurations.

A variety of diagnostic tools were used to investigate the laser-target-ambient interactions (Stamper, et al., 1986, Ref. 4). Although the radius of the expanding shell scales as a classical blast wave (Ripin,

Stamper, McLean, 1984, Ref. 5), a number of non-blast-wave features are evident from the diagnostics. We have modeled the laser-target-ambient interactions with the two-dimensional MHD computer code, MACH2 (Frese, 1987 and Peterkin, et al., 1986, Refs. 6 and 7), and are able to simulate the formation and time-development of the nearly-spherical blast wave (Stellingwerf, Peterkin, Longmire, 1986, Ref. 8).

The most prominent non-blast-wave feature of the expanding bubble seen in diagnostics of the "high pressure" experiments is the aneurysm. It appears as an outward-pointing protrusion attached to the otherwise spherical blast wave. In shadowgraphs from experiments done with the Pharos II facility, the aneurysm appeared at various locations within an imaginary cone of about 30 degree half angle that was centered about the target normal. The laser beam was always at normal incidence to the target. Because the aneurysm appeared to be aligned with neither the the laser beam nor the target normal, the mechanism responsible for its formation was not obvious.

To explain the aneurysm, a number of interesting ideas were put forth. These include:

1. non-uniform laser intensity across the laser spot,
2. a jet of material from the target that catches up with the leading blast front (as suggested by C. Longmire),
3. instability of blast wave induced by thermally generated magnetic fields
4. laser heating of the plasma within the laser path.

We modeled the first of these processes with MACH2, and concluded that it was not the cause of the aneurysm (Stellingwerf, Peterkin, Longmire, 1986, Ref. 8). Subsequently, experiments were done at NRL with the Pharos III facility that employed an ISI-smoothed laser pulse (Lehmberg, Obenschain, 1983, Ref. 9). The aneurysm persisted, thus ruling out a spatially non-uniform pulse as the driving mechanism. As for the second idea, the material that is ablated from the target at late times travels through a region from which ambient gas has been swept away by the

leading blast front. The leading front may be overtaken by later debris. This may explain aneurysms that appear normal to the target when it is illuminated by a low energy laser pulse with non-normal incidence. Such is seen in one of the three NRL experiments done at very low energy with the Pharos III facility. (Experiments 86-582, -583, and -586 were low energy shots; 86-583 shows the feature.) We have modeled thermally generated magnetic fields, the third from this list, with MACH2 (Peterkin, Stellingwerf, 1987, Ref. 10). In a model with parameters from NRL shot 85-544 (109 J with 5 Torr ambient nitrogen), we calculate that less than one percent of the laser energy is converted to magnetic field energy near the target, and this field is convected with the expanding bubble. Our simulations show no disruption of the shell from this magnetic perturbation. Experimental work is under way to investigate the magnitude and location of thermally generated magnetic fields. It has been suggested (Guillani, 1985, Ref. 11) that such fields may explain the turbulent-looking structure that seems to exist in front of the blast wave as seen in shadowgraphs of some experiments with low energy laser pulses.

Clearly, the second and third ideas from the above list deserve further consideration in attempts to explain deviations from classical blast wave behavior seen in laser-target-ambient experiments. In this paper, however, shall limit our discussions to the laser heated channel. We illustrate that if the laser energy is sufficient, an aneurysm will form centered about the laser axis. This idea has been investigated previously (Lyon, 1985, Ref. 12) with a null result. Our two-dimensional modeling shows, however, that laser heating of a narrow channel does cause an aneurysm when the laser energy is at least a few tens of Joules and when the ambient pressure is above a Torr (Stellingwerf, Peterkin, Longmire, 1986, Ref. 8).

Although an aneurysm is always present centered about the laser axis when the laser energy is above a threshold on the order of 10 J in experiments with the new Pharos III facility, small aneurysm-like protrusions are often visible off-axis as well. It seems likely that there is more than a single mechanism responsible for the production of such

features on the shell. However, the experimental reproducibility of the on-axis aneurysm, and our ability to simulate it by modeling a laser-heated channel in the real experimental geometry, suggest that the laser heating of the photoionized plasma in the channel is the driving mechanism for the on-axis aneurysm.

Structure similar to the aneurysm is seen in photographs of the blast from nuclear devices that are suspended from tethered balloons or support towers and stabilized by guy-wires (Jones, Childers, Kodis, 1987, Ref. 13). Called "cable spikes", these conical-shaped protrusions emanate from the expanding blast front along the guy-wires. Cable spikes are thought to be caused by absorption of radiation by the wires and the development of a heated, low density channel (similar to the present case).

In this report the aneurysm is discussed primarily from the viewpoint of the channel heating mechanism, but other physical processes are addressed as well. Section 2 presents motivation, background, and results of several series of two-dimensional MHD simulations that demonstrate aneurysm formation and its dependence on various parameters. In Section 3 a simple channel heating model is developed that explains the detailed MHD results. Section 4 discusses the method of computing self-generated magnetic fields used in the code, while Section 5 shows a their effects in sample computations. Finally, Section 6 shows a preliminary computation of a case with both self-generated fields and an ambient magnetic field parallel to the laser path.

A summary of the experimental and theoretical results of this investigation have been submitted to The Physics of Fluids and should appear in late 1988 or early 1989.

SECTION 2

THE ANEURYSM

2.1 THE CHANNEL-HEATING MECHANISM.

A simple calculation illustrates how the temperature of the gas within the path of a high-irradiance laser can rise from room temperature to many electron Volts. Let us assume that X-rays emanating from the laser-irradiated target singly ionize a fraction of the constituent atoms of the gas nearby during the early stages of the laser pulse. Subsequent laser light is absorbed by the ionized atoms near the target, raising the local temperature substantially. This hot plasma close to the target then itself radiates, ionizing ambient gas nearby in the process. This process cascades outward from the focal spot of the laser. We approximate this complicated radiation transport process by simply assuming the ambient gas is preionized in a manner that falls as the square of the distance from the focal spot. Such $1/r^2$ behavior follows from the spherical divergence of the laser beam. To be precise, our model for preionization is used as a lower bound on the ionization fraction of the ambient medium. The ionization fraction, ζ, decreases with the square of the distance from a point at the focal spot of the laser and is normalized to have the value, ζ_0, at a distance one cm from that point. We tried various values of ζ_0 and conclude that a value of five percent gives results most consistent with experiment. This value, however, is thought to be higher than that of reality.

In a distance, dr, some fraction of the laser light is absorbed by the free electrons via inverse bremsstrahlung. The fractional power absorption (Johnston and Dawson, 1973, Ref. 14), f, in mks units with temperature in eV, is:

$$f = 1 - \exp\left[-\int \frac{\alpha\, b\, \zeta'\, \ln\Lambda}{\lambda^2\, T^{3/2}} \frac{x^2\, dr}{\sqrt{1 - x}}\right] \qquad (1)$$

where α is the constant $1.0779\ 10^{-5}$, b is taken to be 0.5, ζ' is the larger of the fractional ionization, ζ, and unity, ln Λ is a Coulomb logarithm (of order unity), λ is the laser wavelength in meters, T is the temperature in eV, x is the dimensionless ratio of the electron number density to the critical number density, and dr is an increment in the direction of laser propagation. The laser light that arrives at the critical surface is absorbed there. If the integrand in Equation (1) is small and $x \ll 1$ (that is the case in low density regions), the absorption coefficient is:

$$\kappa_\nu = \alpha \frac{b\ \zeta'\ \ln \Lambda\ x^2}{\lambda^2\ T^{3/2}} \tag{2}$$

which can be written as

$$\kappa_\nu = \beta\ b\ \lambda^2 \frac{\zeta'\ \zeta^2\ \rho^2\ \ln \Lambda}{A^2\ T^{3/2}} \tag{3}$$

where β is $3.133\ 10^{18}$, ρ is the mass density, and A is the atomic weight of the plasma. If a fraction, κ_ν, of the incident laser power, P_0, that passes through a disk of radius r and density ρ is absorbed per unit length by that disk, the temperature change is:

$$\frac{dT}{dt} = \frac{\kappa_\nu\ P_0}{\rho\ \pi\ r^2\ c_v} \tag{4}$$

where c_v is the specific heat of the material. If we assume an ideal gas equation of state, the specific heat is

$$c_v = 1.44\ 10^8\ \frac{(1 + \zeta)}{A} \quad \frac{\text{Joule}}{\text{eV-kg}} \tag{5}$$

independent of the temperature, and we can estimate the size of the temperature rise for some particular values of the parameters. Equation 5 does not take into consideration the energy that ionizes rather than heats the plasma. The ionization energy is in general not negligible (see Section 3, Figure 20). Combining Equations (3), (4), and (5), we have

$$\frac{dT}{dt} \approx \frac{\gamma\, b\, \lambda^2\, \zeta'\, \zeta^2\, \rho\, \ln \Lambda\, P_0}{r^2\, A\, T^{3/2}\, (1 + \zeta)} \tag{6}$$

where $\gamma = 6.925\ 10^9$. If ζ', ζ, ρ, $\ln \Lambda$, and r are approximated as time independent quantities, we can integrate Equation (6). The time integral of the incident laser power is the incident laser energy, E_0. We then have for the final electron temperature, T_f, after a time interval, t

$$T_f = [T_0^{5/2} + \frac{5}{2} (\frac{\gamma\, \lambda^2\, \zeta'\, \zeta^2\, \rho\, \ln \Lambda\, b\, E_0}{r^2\, A\, (1 + \zeta)})]^{2/5} \tag{7}$$

where T_0 is the initial temperature.

Let us try to estimate the temperature rise in the laser channel for NRL experiment 85-544. Dark field shadowgraphs from this experiment show a well-formed aneurysm centered along the laser axis as illustrated in Figure 1. A 109 J laser beam propagates through room temperature Nitrogen gas at 5 Torr pressure. This corresponds to a mass density of $8.2\ 10^{-6}$ gm/cc, which if five percent ionized (five percent of the ions are singly ionized) at a distance of 1 cm above that focal spot of the laser produces an electron number density of $8.77\ 10^{15}$/cc. The laser is focused to a circular spot approximately 100 μm in radius, and the beam converges to this spot with an angle of 2.86 degrees from the target normal (as illustrated in Figure 2). At a distance one cm from the focal spot, the radius of the laser disk is almost 600 μm and the cross sectional area of the ambient gas that is pierced by the laser beam there is a larger than the laser focal spot by a factor of 36. During the first half of the

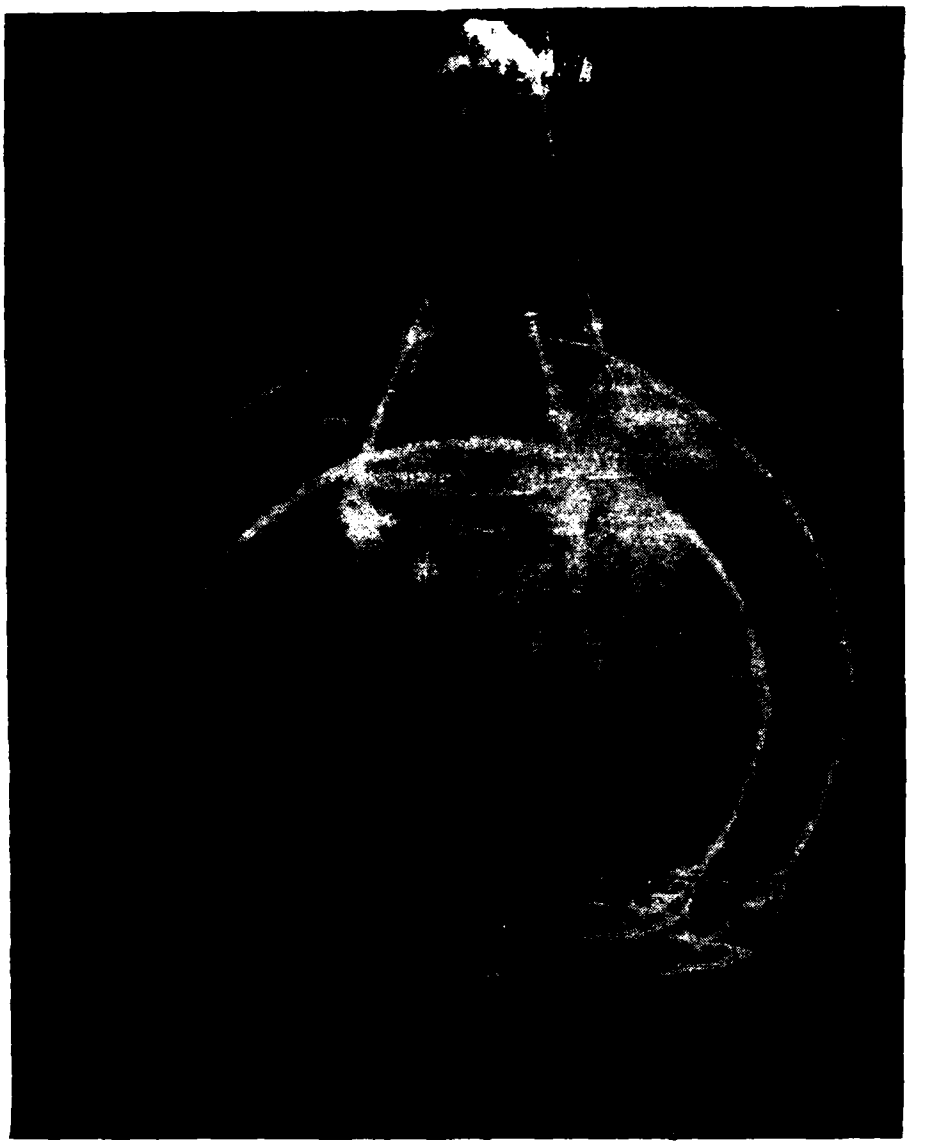

Figure 1. Dual time shadowgram (71 ns and 140 ns) of NRL 85-544.

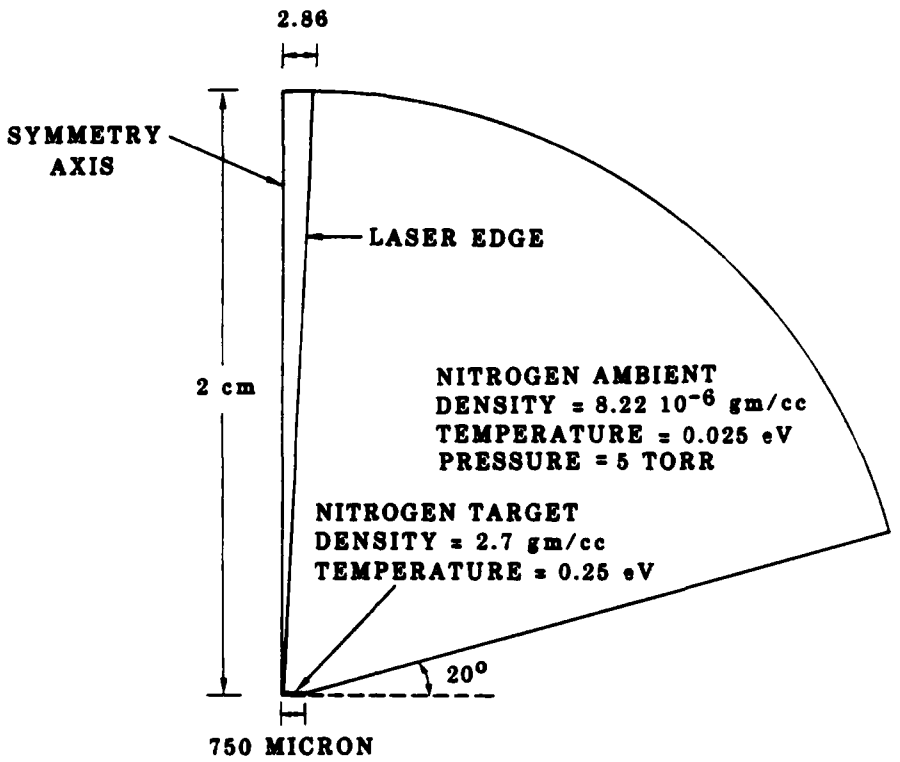

Figure 2a. Outline of the calculation mesh for MACH2 simulation, showing dimensions. The target region is enlarged in Figure 2b.

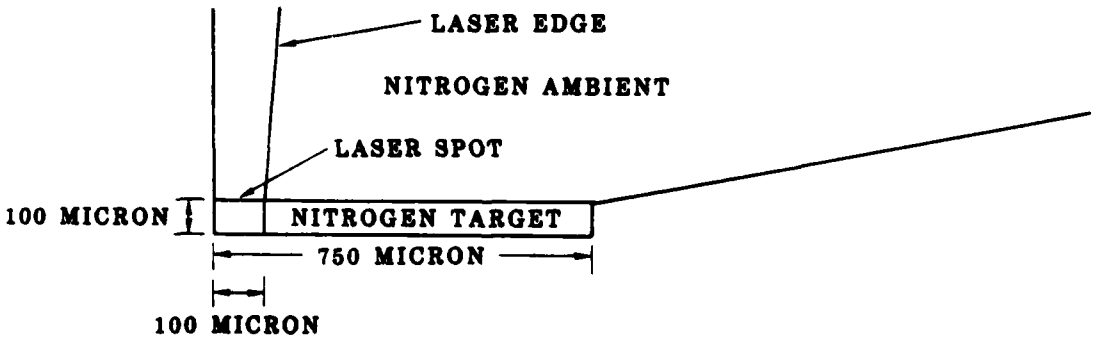

Figure 2b. Outline of the target region for MACH2 simulation, showing dimensions.

pulse, 54.5 J of energy is incident on any slice of the ambient gas if $f \ll 1$. From Equation (7), we can estimate as a lower limit that the temperature of a plasma slice 600 μm in radius will rise from room temperature to be on the order of 1.33 eV if an ideal gas specific heat is assumed and if the ionization and mass density are assumed to be almost constant. At this density, nitrogen is fully ionized at 100 eV. If we assume full ionization and calculate $\ln \Lambda$ to be 3.3, we find an upper limit of 108 eV on the temperature 1 cm from the target. Clearly, a self-consistant model that takes the ionization into account is required to accurately estimate the temperature rise in the channel. Because of the strong focusing of the laser beam, laser energy density, and hence the change in temperature of the gas, are expected to vary essentially with the inverse of the cross-sectional area of the beam. If we use our simple model to estimate the rise in temperature of the gas at the focal spot of the laser--where the intensity is 36 times as large as it is 1 cm away--we obtain roughly 3 KeV as an upper limit on the temperature at the target.

Our estimate for the fraction of the incident power absorbed 1 cm from the laser focal spot is rough because as the temperature rises a few tens of eV, the fractional ionization does change appreciably (the average nitrogen atom in a 5 Torr, 5 eV plasma is twice ionized). As the temperature rises so does the fractional ionization, but as the heated plasma expands its density falls. Because the fraction of the laser energy that is absorbed by the medium increases as the fractional ionization rises, but decreases as the temperature rises and the density falls, a linear analysis is not sufficient to determine the exact nature of the laser channel. Clearly, though, additional heating of a fully ionized material will serve to decrease the fractional absorption as the temperature increases.

These effects are included in a more comprehensive model in Section 3 of this report. The present results clearly indicate channel heating will be an important process, and justify detailed numerical models to verify this conclusion.

2.2 TWO-DIMENSIONAL MODELS.

We have performed 2 1/2 dimensional computer simulations of the NRL laser-target-ambient system with MACH2, an MHD code which is described in detail elsewhere (Frese, 1987, and Peterkin, et al., 1986, Refs. 6 and 7). Briefly, MACH2 is a single fluid, single temperature MHD code that carries all three spatial components of vectors, but allows no quantity to depend on the azimuthal coordinate when it models cylindrically-symmetric problems. Accurate equations of state that assume local thermodynamic equilibrium are used by accessing SESAME tables at Los Alamos National Laboratory (LANL) during each computational cycle. The ions and electrons are assumed to be in equilibrium and hence are characterized by a single temperature. The net charge in any cell is zero. The code solves the following equations in MKSA units in a fractional time-split manner:

Magnetic Induction

$$\frac{\partial \vec{B}}{\partial t} = \nabla \times (\vec{v} \times \vec{B}) - \nabla \times (\eta \nabla \times \vec{B}) + \frac{1}{e} \nabla \times \left[\left(\frac{1}{n_e + n_i}\right) \nabla P\right] - \nabla \times \frac{1}{e n_e} (\vec{J} \times \vec{B}) \tag{8}$$

Fluid Momentum

$$\rho \frac{\partial v^i}{\partial t} = - \rho v^j \nabla_j v^i + \nabla_j \left(-P g^{ji} + \sigma^{ji} + \frac{1}{\mu_0} (B^j B^i - \frac{1}{2} B^2 g^{ji})\right) \tag{9}$$

Specific Internal Energy

$$\rho \frac{\partial \varepsilon}{\partial t} = - \rho \vec{v} \cdot \nabla \varepsilon + (-P g^{ji} + \sigma^{ji}) \nabla_i v_j + \eta \mu_0 J^2 - \frac{1}{e(n_e + n_i)} \vec{J} \cdot \nabla P + \nabla \cdot (\kappa \nabla T) - a \rho \chi T^4 + f P_l \tag{10}$$

Mass Continuity

$$\frac{\partial \rho}{\partial t} = -\nabla \cdot (\rho \vec{v}) \tag{11}$$

In the above, $\vec{B}$ is the magnetic induction, μ_0 the permeability of free space, $\vec{v}$ the fluid velocity, η the electric diffusivity (electric resistivity divided by μ_0), n_e and n_i the electron and ion number densities, P the thermal pressure, ρ the mass density, σ^{ji} the viscous stresses, ε the plasma specific internal energy, T the temperature, $\vec{J}$ the current density ($(1/\mu_0)$ curl $\vec{B}$), κ the thermal conductivity, e the magnitude of the charge of an electron, g^{ji} the spatial metric, χ the Planck mean opacity (cross-section per unit mass), a Stephan's constant, P_l the instantaneous laser power per unit volume at infinity, and f the fractional absorption given by Equation (1).

The code is axisymmetric with the axis of symmetry appearing as a vertical line to the left in computer-generated pictures. Rotation about this axis is assumed. The MACH2 simulations discussed herein take place on numerically-generated Eluerian meshes. The difference equations are of the finite volume type which is well suited to non-rectangular meshes required for problems with complex shapes.

Results from four MACH2 calculations of a focused laser pulse interacting with the partially ionized gas are illustrated in Figure 3. In this figure we plot the temperature on a log scale as a function of distance from the laser focal spot through a slice down the laser channel. To simplify our computations, we modeled only the ambient gas (without a solid target) in each of the simulations. The sole difference among these simulations is the degree of preionization. Recall that our model for preionization decreases with the square of the distance from that focal spot. Four values for the initial fractional ionization at 1 cm from the focal spot were chosen (one percent, three percent, five percent, and ten percent). The temperature rises to approximately 600 eV at the laser focal

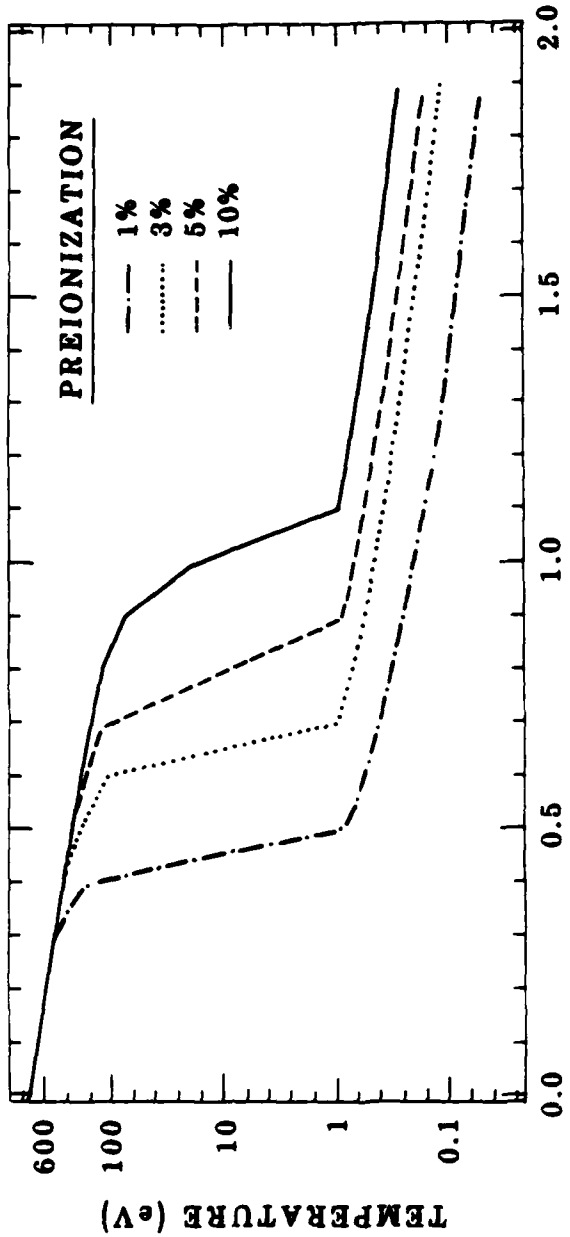

Figure 3. Temperature at 4 ns (time of peak laser power) versus distance from focal spot for a 5 Torr preionized plasma (with 4 distinct values) without a target.

spot (where the laser intensity is 6 10^{13} Watt/cm^2) in each of these simulations. The front of the temperature gradient is further from the focal spot as the amount of preionization is increased. For example, 54.5 J from a laser raises the temperature in the channel 1 cm from the focal spot to almost 1 eV when the initial ionization fraction is five percent there (not inconsistent with the previous analysis), but to only 0.25 eV when the initial ionization fraction is one percent. The front of the hot channel extends further from the focal spot as the degree of preionization increases. By varying the preionization in simulations with a target in place, we have found that it is necessary for the hot channel to extend beyond the blast wave at early times if an aneurysm is to form.

The physics is further complicated when a dense target is present to absorb the large fraction of the laser energy that is not absorbed in the ambient gas. Figures 4a-c illustrate a simulation of NRL shot 35-544, complete with a target at the focal spot of the laser, where we have preionized the ambient nitrogen to a level of five percent 1 cm from the target surface. As seen in the 10 ns picture, Figure 4a, the hot shell within the channel (where the temperature is 0.45 eV) extends 1.53 cm from the target. The expanding bubble is substantially behind at this time--a distance of 0.6 cm from the target surface. The target surface is hot (610 eV) at 10 ns, but cools to 60 eV at 71 ns. Figures 4b (at 30 ns) and 4c (71 ns) illustrate that the shell gets closer to the temperature front as time progresses. However, the large separation at early times allows an aneurysm to begin to form. The aneurysm is clearly defined by 71 ns. The velocity picture at this time shows a jet of high velocity material confined to the region near the axis. The electron number density contours are closely spaced at the location of the shell. It is this shell, the locus of points at which there are large gradients in electron number density, that is to be compared to shadowgraphs of the experiments. The aneurysm, while evident in Figure 4c, is not quite as large as that seen in the experiment at 71 ns.

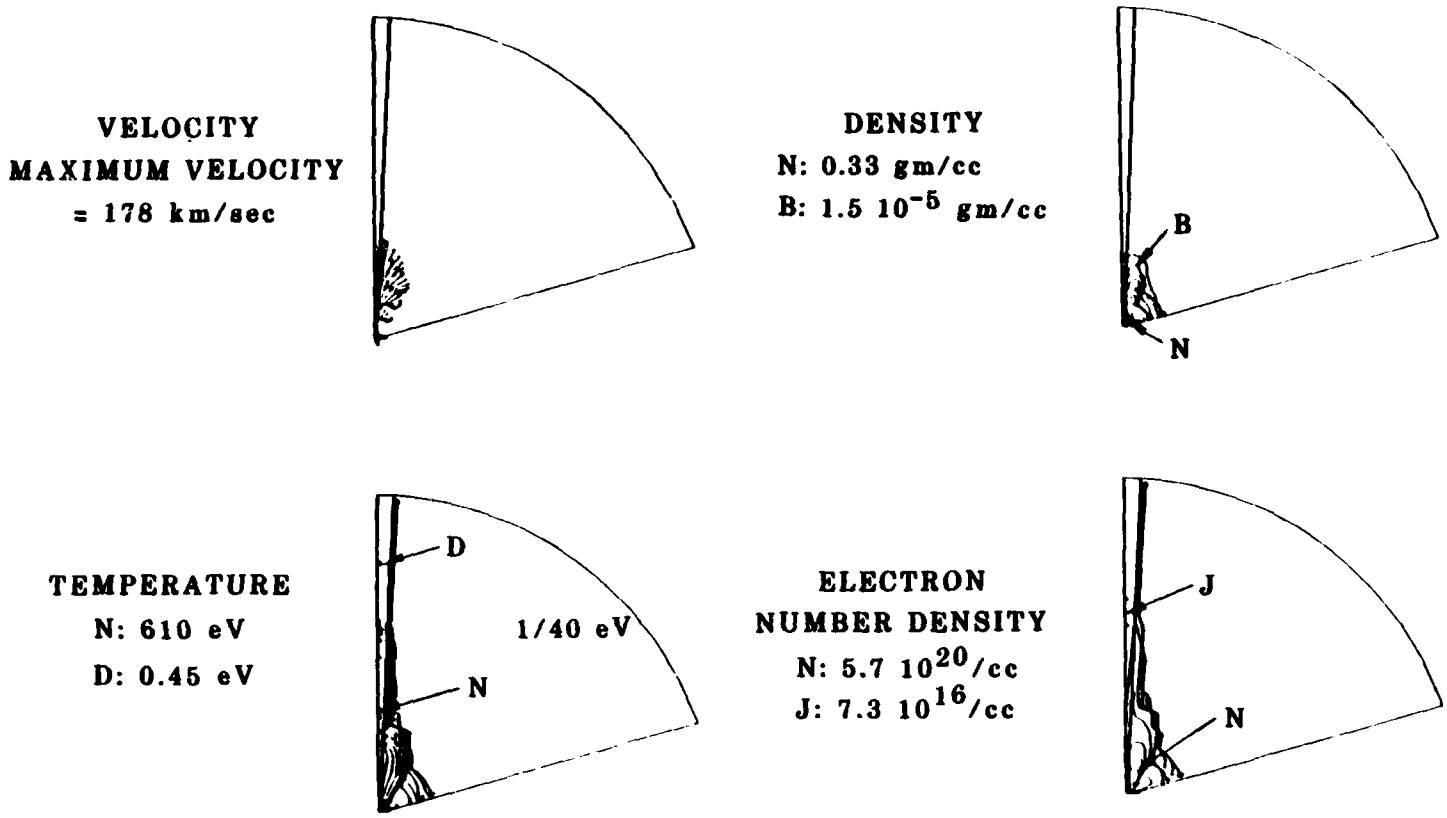

Figure 4a. Velocity, density, temperature, and electron number density pictures at 10 ns. Flat laser pulse; 5 percent preionized 1 cm from the target.

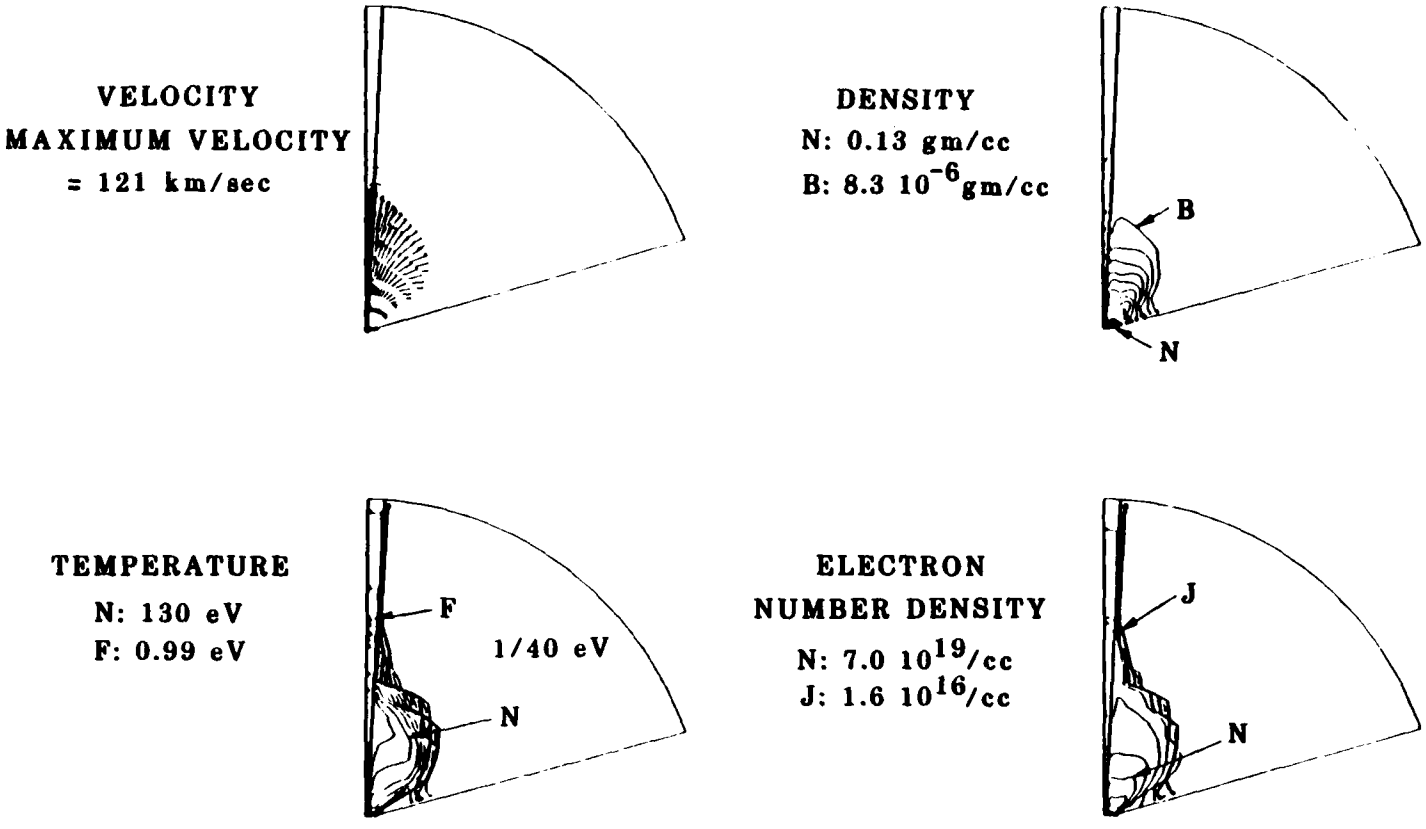

Figure 4b. Velocity, density, temperature, and electron number density pictures at 30 ns. Flat laser pulse; 5 percent preionized 1 cm from the target.

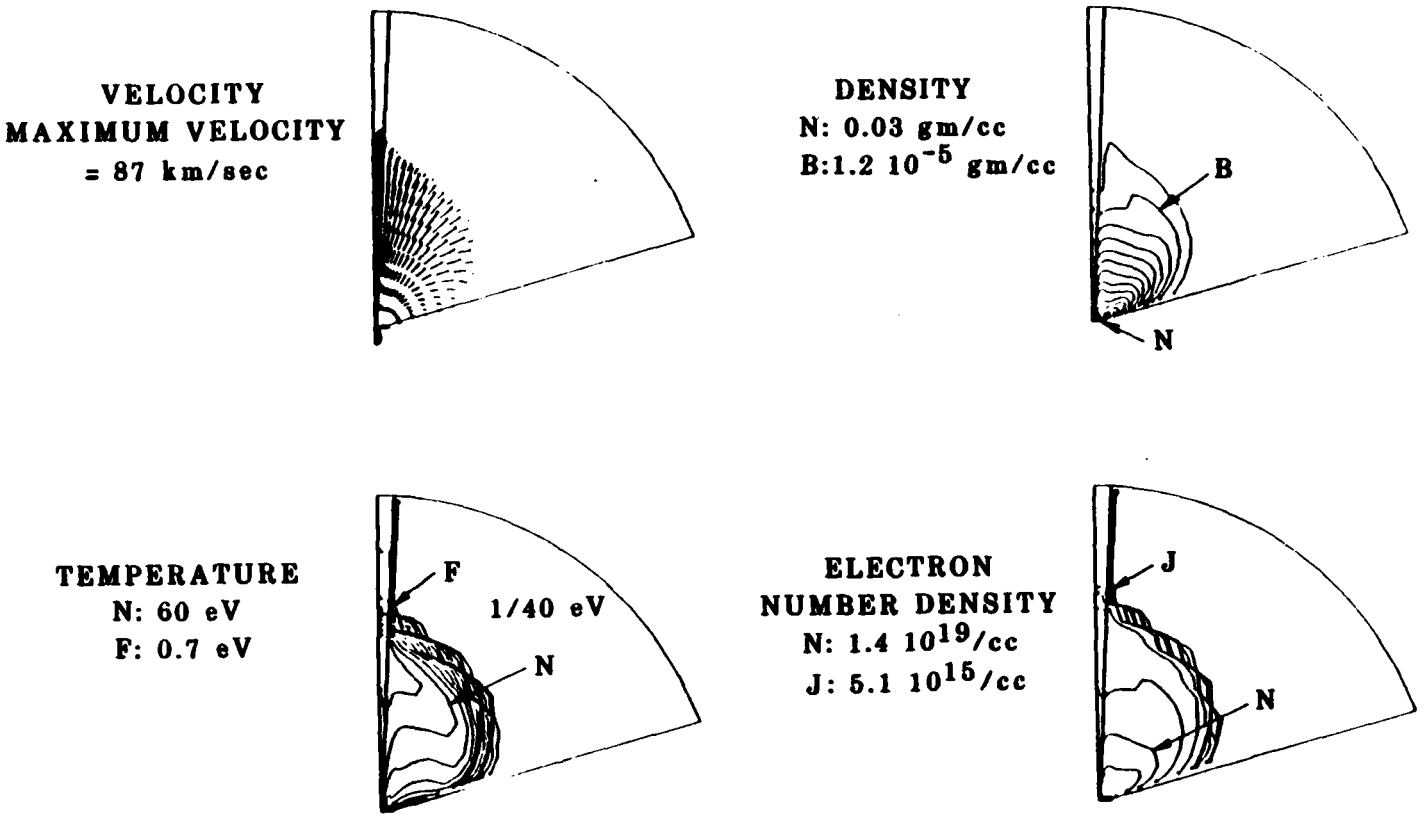

Figure 4c. Velocity, density, temperature, and electron number density pictures at 70 ns. Flat laser pulse; 5 percent preionized 1 cm from the target.

Heating of the narrow laser channel induces a weak cylindrical shock as material flows radially outward. Consider a particular location some distance from the target surface. If the density at that axial location in the channel falls before debris from the laser-ablated target reaches that location, the debris will advance more rapidly in the axial direction within the semi-evacuated laser channel. Without increasing the total laser energy, a hotter channel, and hence a stronger cylindrical shock, is obtained with a larger initial fractional ionization of the ambient medium. Figure 5 shows accumulated energy as a function of time for the duration of the 109 J laser pulse. Slightly less than 0.1 J from the incident laser energy is absorbed in the channel. The channel is here defined as that material with mass density less than twice the ambient density of $8.2\ 10^{-6}$ gm/cc that is in the path of the laser. Of course, simulations with no preionization (and hence no absorption of laser energy by the ambient medium) produce spherical blast fronts without aneurysms.

Figure 6 illustrates electron number density and plasma velocity in the region close to the target on a finely-zoned grid at 2 ns intervals for the first 10 ns of the simulation. One can see clearly the formation of the laser-heated channel outside the expanding blast front, and a jet of plasma moving ahead of the blast inside the channel.

We have chosen not to compute the effects of radiation cooling on the hot plasma for the simulations discussed in this section, so the temperature of hot spots are too large. This defect should not change the conclusions concerning the laser-heated channel. Our computations show that the laser channel is not significantly heated by thermal conduction from hot regions near the target. Thermal conduction from an essentially point target would not be confined to a narrow channel, but would isotropically heat the ambient medium.

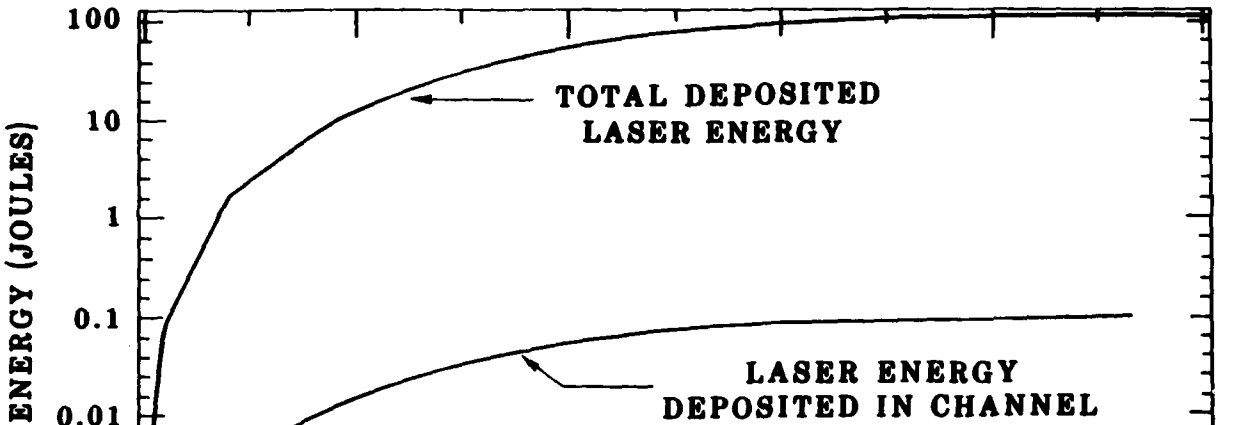

Figure 5. Laser energy versus time for MACH2 simulation of NRL 85-544.

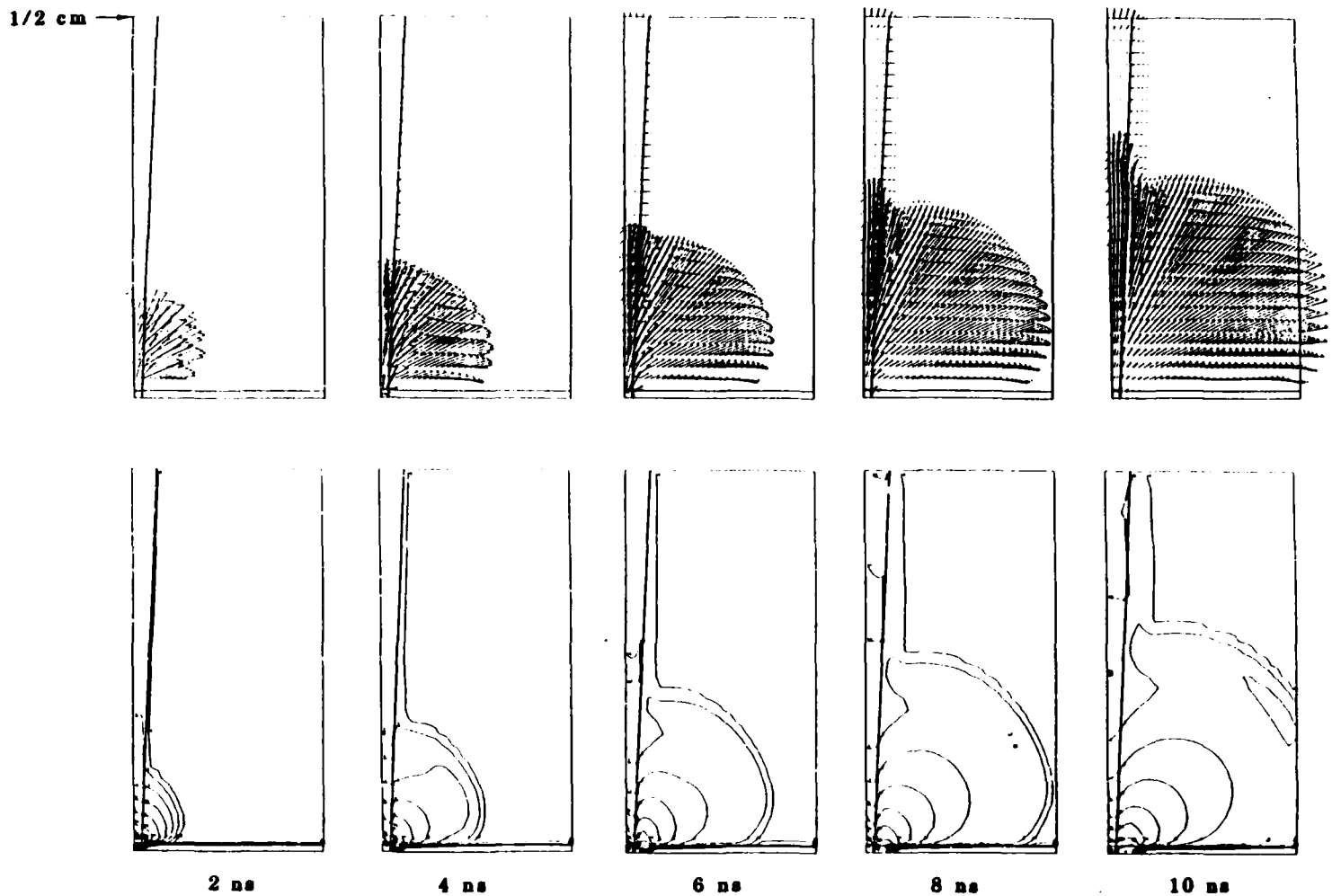

Figure 6. Velocity and electron number density close to the target for MACH2 simulation of NRL 85-544 (model L112).

The issues of radiative cooling and thermal conduction are addressed via numerical simulation in the next section. However, we can estimate analytically the importance of thermal conduction over large length scales. Conduction of heat energy from hot regions obeys a temperature diffusion equation

$$\frac{\partial T}{\partial t} = \frac{1}{\rho C_v} \nabla \cdot (\kappa \nabla T) \tag{12}$$

where we assume Spitzer conductivity, κ, that is proportional to $T^{5/2}$. In addition, thermal flux is limited to some fraction, τ, times the energy flux carried by free-streaming electrons, i.e.,

$$\kappa \nabla T \leq \tau u v \tag{13}$$

where τ is often taken to be 0.4, u is the electron internal energy density, and v is the electron thermal speed. The Spitzer thermal conductivity for a 500 eV plasma is approximately $3.6\ 10^9$ J/m-sec-eV. On length scales of 1 mm, the time scale for thermal conduction near the target where the density is $3\ 10^{-3}$ gm/cc is 60 ns. This is long compared to the laser pulse length, so thermal conduction in the hot, moderately dense region near the target is not expected to be a dominant effect.

The debris/air interface outside the laser channel lies, at a particular time, at the radius of a blast wave that emanates spherically from a point source according to the similarity relation (Zel'dovich, Raizer, 1966, Ref. 15):

$$r(t) = f(\gamma) \left(\frac{E}{P}\right)^{1/5} t^{2/5} \text{ cm} \tag{14}$$

for energy (E) in Joules, ambient pressure (P) in Torr, and time (t) in ns. $f(\gamma)$ is a function of the adiabatic index and is generally of order 0.1. The NRL experiments fit Equation (14) with $f(\gamma) \approx 0.123$ (Ripin, Stamper,

McLean, 1984, Ref. 5). For a 109 J laser and 5 Torr ambient pressure, the radius of the blast front at 70 ns is 1.25 cm. To facilitate a comparison between the MACH2 simulation and experiment, we display a digitized plot of the shadowgraph for NRL shot 544 in Figure 7a. In Figure 7b, we display the contour plot of the electron number density from the simulation with five percent preionization, drawn to the same scale as the shadowgraph. The MACH2-simulated location of the debris/air interface away from the axis agrees with that of the experiment. Further, this location, estimated from Figures 7a and 7b to lie 1.2 cm from the target surface, agrees with that predicted from the blast wave equation. The location and size of the central aneurysm simulated by MACH2 looks remarkably like that produced by the experiment. Figure 8 is a superposition of the digitized version of the NRL shadowgraph and the electron number density contour plot from MACH2. We speculate that numerical diffusion in our Eulerian calculations together with the lack of resolution in the laser channel (recall that there are but 4 cells radially through the channel) causes the MACH2 simulated aneurysm to be flattened at its tip rather than to protrude as far from the target as the experimentally generated aneurysm.

Aneurysms were seen in most high-energy experiments done with ambient pressure above 1 Torr. Figure 9 is a shadowgraph of NRL shot 86-625 taken early, 14 ns after peak laser power. The plastic (CH) target was in a nitrogen medium at 5 Torr. The laser pulse τ_{fwhm} was 3 ns and delivered 238 J towards a focal spot of 500 μm radius. The pulse was ISI smoothed and produced a cylindrical shock about the laser axis as seen in the picture. We simulated this NRL shot with MACH2, again assuming five percent preionization 1 cm from the focal spot, and placed 8 computational cells across the laser spot. Figure 10 shows the electron number density from the simulation at the same time as the shadowgraph in Figure 9. The simulation shows a laser-induced channel similar to that seen in the experiment. Figure 11 is a superposition of a digitization of the shadowgraph and the simulation, drawn to the same scale.

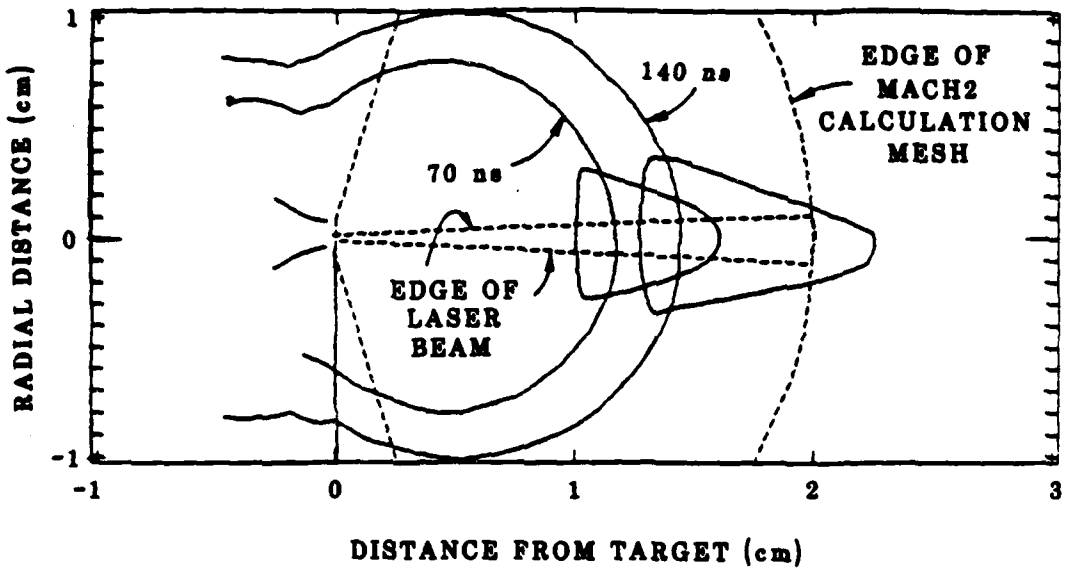

Figure 7a. Digitization of NRL laser/HANE shadowgraph for shot 85-544 showing shell and aneurysm at 70 and 140 ns.

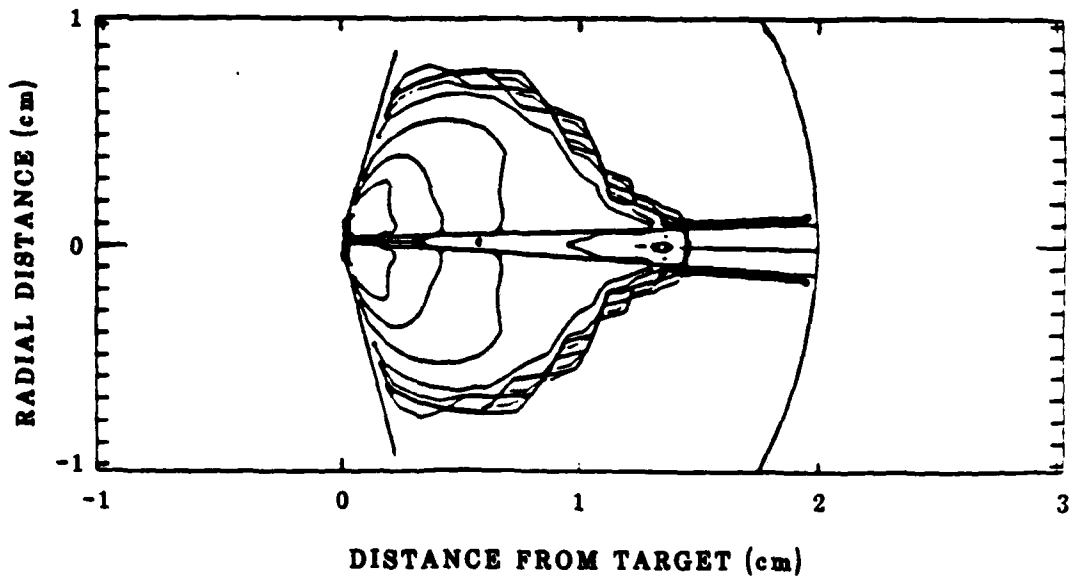

Figure 7b. Contour plot of electron number density at 70 ns for MACH2 simulation of NRL shot 85-544.

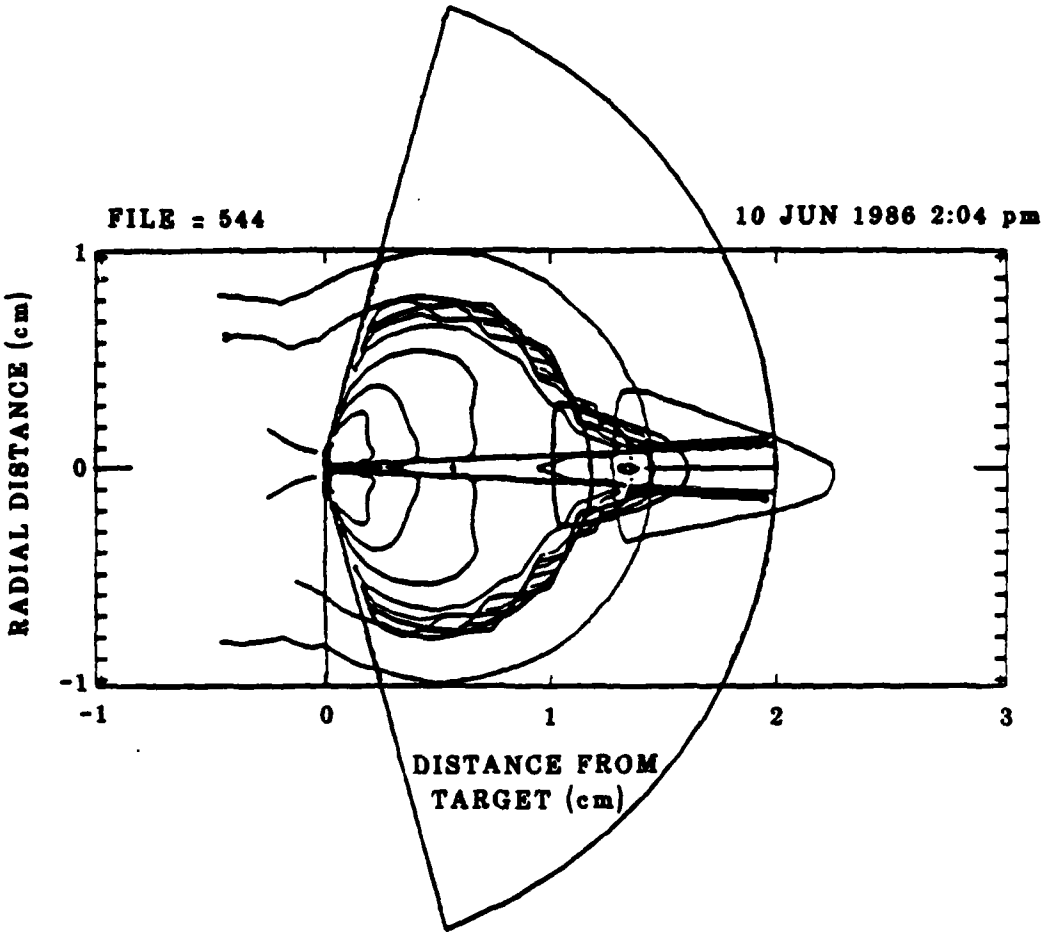

Figure 8. Figures 7a and 7b superimposed.

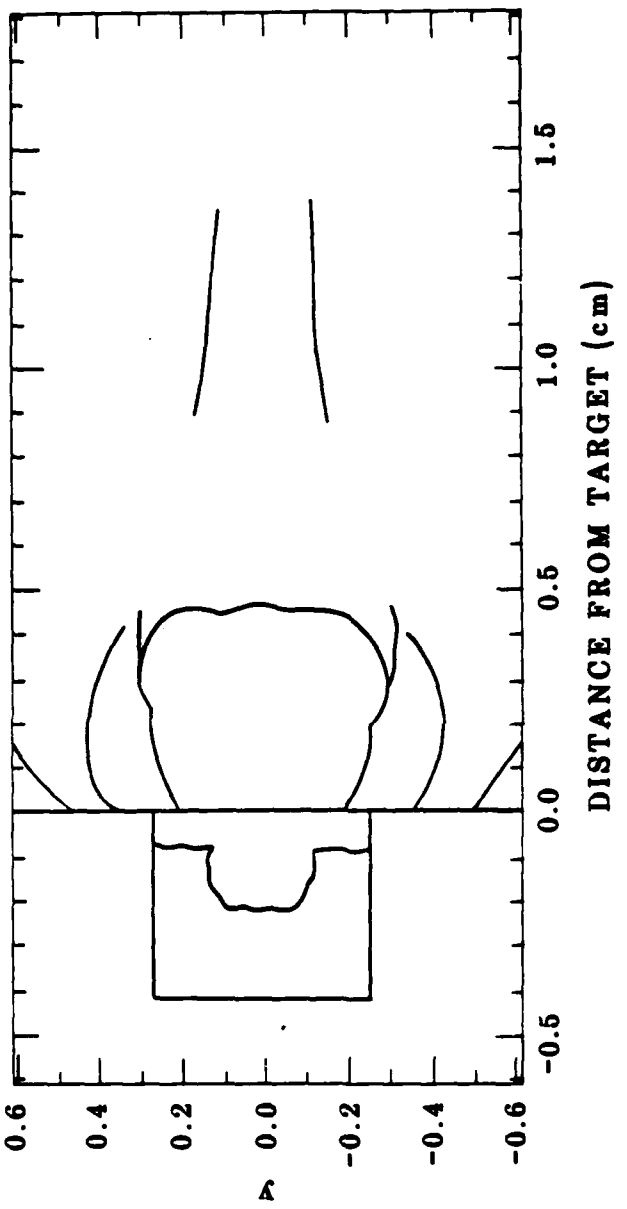

Figure 9. Digitization of the shadowgram of NRL 86-625 at 14 ns.

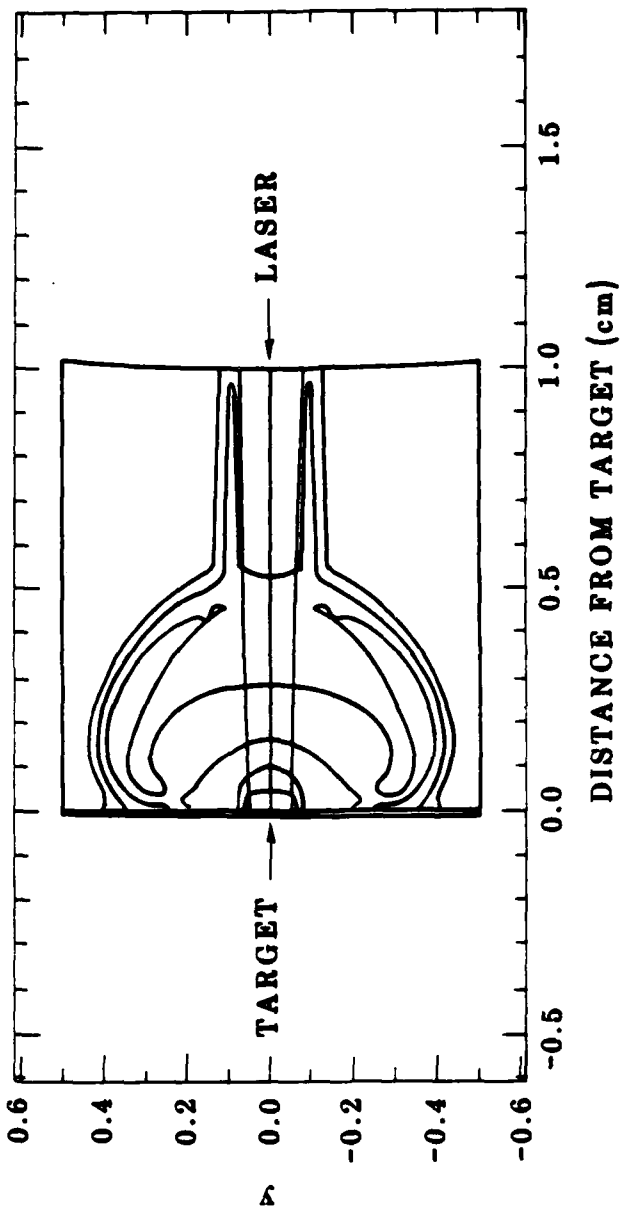

Figure 10. Electron number density from MACH2 simulation of NRL shot 86-625 at 14 ns.

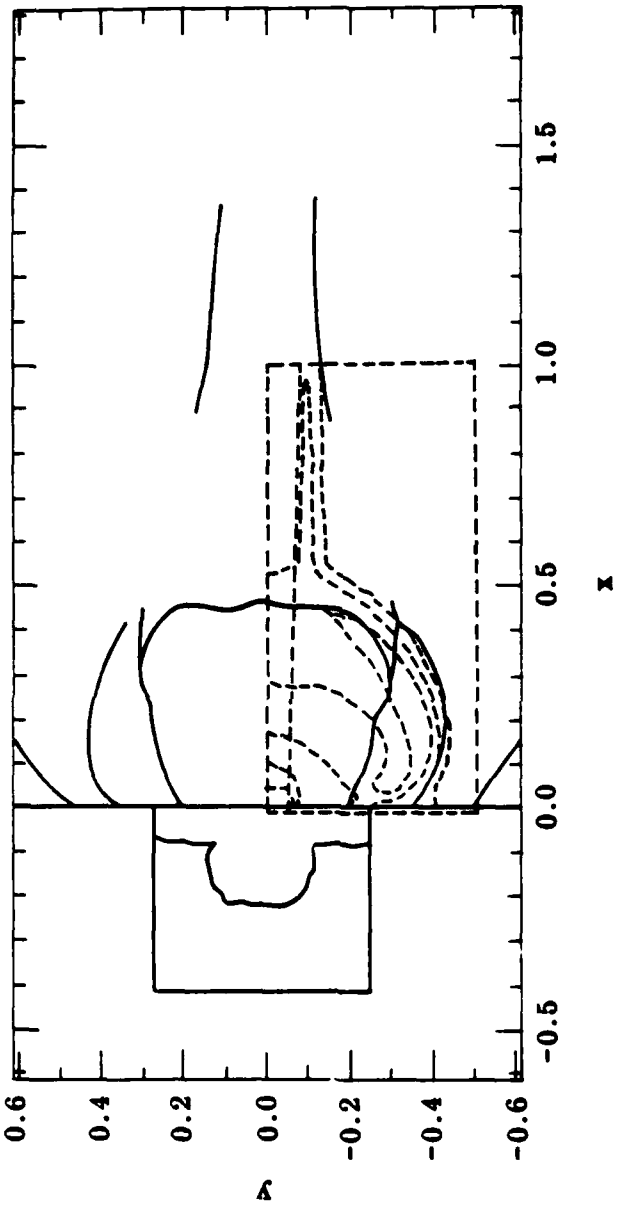

Figure 11. Superposition of Figures 9 and 10.

The laser axis and the target normal coincide in most NRL experiments of relevance to us. There are a few exceptions, however. Figure 12 is a shadowgraph from NRL shot 86-581 taken at 59 ns after peak power. The beam, carrying 95 ISI-smoothed Joules, strikes the target 30 degrees from the target normal. The aneurysm is centered about the laser axis--not the target normal.

2.3 EFFECTS OF VARIOUS PHYSICAL PROCESSES ON ANEURYSM FORMATION.

The purpose of this section is to investigate the effects of some of the physical processes that occur in the laser-ambient-target system and that may affect the partially ionized channel that causes aneurysm production and development.

A possible criticism of our earliest models of the laser-ambient-target system (Stellingwerf, Peterkin, Longmire, 1986, Ref. 8) is that both the target and the ambient consisted of a single material. The earliest models included a target and an ambient medium both composed of aluminum. Room-temperature gaseous aluminum does not exist at 5 Torr, so our model for the equation of state was certainly suspect. Subsequent models, including those discussed in Section 2.2, included a nitrogen medium and a cryrogenic nitrogen target. These models are reasonable because the equation of state for the ambient nitrogen is undoubtedly correct given our assumption of local thermodynamic equilibrium, and the target material that is dynamic in the simulation is heated to KeV temperatures early in the simulation and becomes a fully ionized nitrogen plasma and hence not unlike aluminum plasma. As target material expands in and behind the blast front, it adiabatically cools to tens of eV. In this region of phase space, the differences between Al and N may be noticeable. Of course the radiation spectrum is quite different for these two materials, but this is not of consequence for our models that lack sophisticated radiation transport. To ameliorate the inadequacy of a model with a single material, we added to MACH2 the ability to transport distinct materials across an Eulerian calculation mesh. The differences between the results from multi-material and single material simulations are not significant, so earlier conclusions

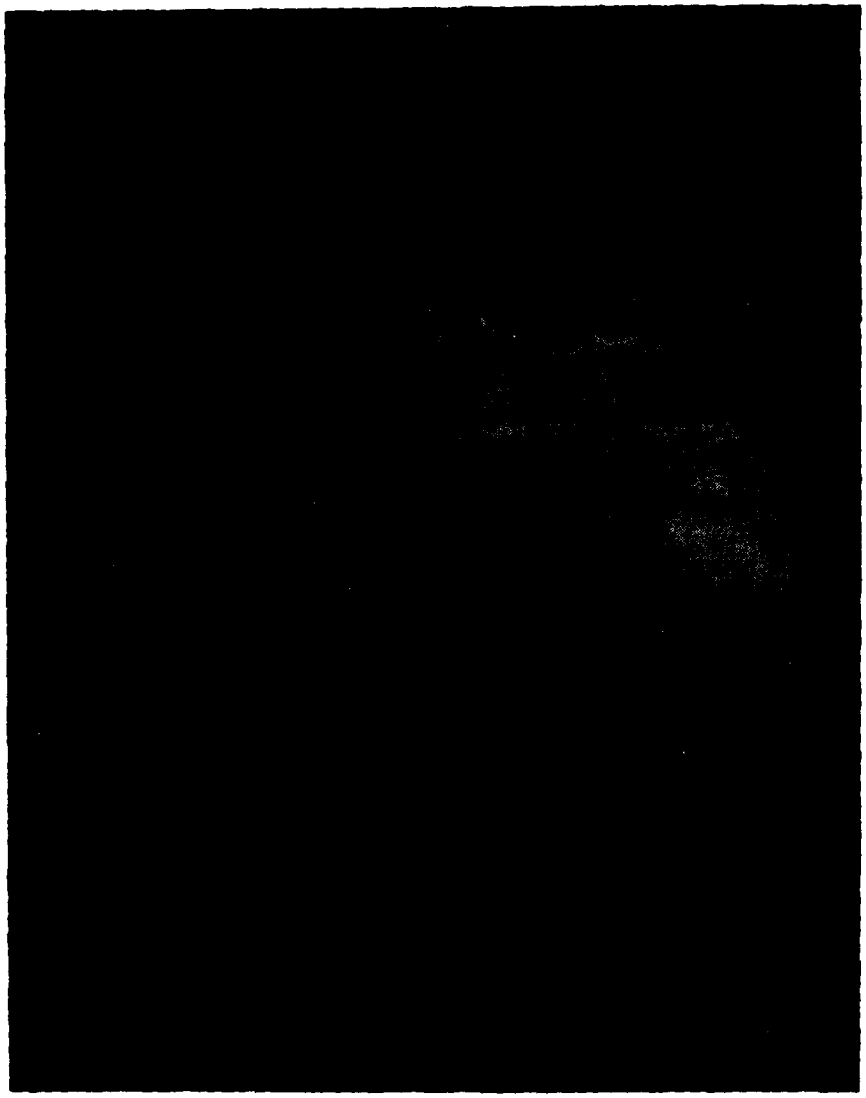

Figure 12. Shadowgram at 59 ns of NRL shot 86-581. Aneurysm is aligned with laser beam and is 30° from the target normal.

concerning the blast front and the aneurysm remain unchanged. The benefits of two-material simulations are two-fold. The approximate position of the debris-air interface is now predicted by the simulations, and the inclusion of distinct materials allows the attention of the reader to be focused on the most important physical issues.

An additional criticism levied against our earliest models addressed our neglect of thermal conduction. Earlier versions of MACH2 contained an explicit treatment of the thermal diffusion process. This treatment required the entire simulation to progress at the numerical thermal diffusion timestep if that timestep was the smallest in the problem. In our models of a high-intensity laser interacting with a solid target, the target achieves temperatures in excess of 1 KeV. Within the Spitzer model for a fully ionized plasma, the thermal conductivity is proportional to $T^{5/2}$. From the thermal diffusion Equation (12), we extract an explicit timestep for this process, dt_{therm}:

$$dt_{therm} = \rho\, C_v\, \ell^2 / \kappa \approx 10^{-13} \text{ sec} \qquad (15)$$

where C_v is the specific heat (which we take to be approximately 0.77 10^8 J/(eV-kg)) when the temperature is on the order of 1 KeV (for which $\kappa \approx 5\ 10^{10}$ J/(m-sec-eV)) and the density is 10^{-4} gm/cc on a mesh with linear cell dimension, ℓ, of 25 micron. Computing at this timestep for the 10 ns laser pulse would require 10^5 computational cycles. At a typical MACH2 rate of 150 cycles per CRAY X-MP cpu-minute, such a computation would require over 10 hours of cpu or 2 orders of magnitude greater than otherwise required by the other physical processes modeled by MACH2. This is clearly undesirable. Hence, we neglected thermal conduction in our earliest models.

To ameliorate this shortcoming, we added an implicit multi-grid treatment (Brandt, 1977, Ref. 16) for thermal conduction to MACH2. This treatment, similar to our existing model for magnetic field diffusion,

allowed us to compute at large thermal Courant numbers. This implicit treatment allowed us to achieve the quasi steady-state solution to the thermal diffusion elliptic equation without a severe computational cost. The results of simulations that include thermal diffusion are discussed below.

In addition, we investigated some other physical processes that have been thought at various times to be of possible consequence to aneurysm production. We have, in the numerical laboratory, the luxury of choice when investigating a physical process. We have varied the degree of preionization of the ambient medium, investigated the effect of thermally generated magnetic fields, allowed the low-density ambient medium to radiate energy without reabsorption, included a 1 Tesla ambient magnetic field, and varied our model for thermal conduction. Our model for the thermal conduction includes the suppression of the thermal conductivity in the direction orthogonal to a strong magnetic field. Thermal energy is carried by electrons, and their mobility in a direction perpendicular to a magnetic field is suppressed as the electrons gyrate about the field lines. The electron gyro-radius is inversely proportional to the magnetic induction, so thermal conduction is most suppressed in regions of the strongest field strength. In Section 5, we shown that the magnetic fields that arise from thermal energy are large, on the order of tens of Tesla, near the edge of an intense laser beam. These fields are anisotropic, and hence, may effect the conduction of energy via electrons from hot regions. This anisotropy may effect the time development of the blast front and the associated aneurysm. The results of these interesting simulations are discussed below. Discussion of the effects of an ambient magnetic field is deferred until Section 6.

Our parameter search is by no means complete. We have not, for example, investigated with our two-dimensional code the effect of ambient pressure on the aneurysm, nor have we investigated the effect of target thickness. The size of the laser focal spot and the magnitude of the incident laser energy has not been varied. Our modest parameter search includes 12 numerical simulations that are described and compared below.

All simulations discussed in this section model the interaction between a 1.06 micron laser beam that delivers 109 J to a solid Al target through a 5 Torr ambient medium of dry air which is 80 percent N_2. The half convergence angle of the beam is 2.86 degree. The laser pulse endures for 8 ns, and peaks at 4 ns with an essentially Gaussian temporal profile. These parameters correspond nominally to the NRL shot 85-544 with the Pharos II facility, and are the same as those simulations discussed in Section 2.2. The spatial character of the beam is uniform with a discontinuous drop to zero intensity at the edge of the beam. Previous research (Stellingwerf, Peterkin, Longmire, 1986, Ref. 8) indicated that a spatially non-uniform laser beam does not strongly affect the character of the aneurysm in the absence of a model for thermally generated magnetic fields. The attributes of the twelve simulations discussed in this section are tabulated below. For each, the computational region measures 1/2 cm × 1/4 cm.

Table 1. Parameters that denote the various physical processes for the 12 models discussed in Section 2.3.

Model Number	Fractional Ionization	Thermal Conduction	Radiation Cooling (1)	sgmf (2)	Other
1	0	on	off	off	
2	0.25 %	on	off	off	
3	1 %	on	off	off	
4	3 %	on	off	off	
5	5 %	on	off	off	
6	5 %	on (3)	off	off	
7	5 %	off	off	off	
8	5 %	on	on	off	
9	1 % (4)	on	off	off	
10	5 %	on	off	off	no target (5)
11	5 %	anisotropic (6)	off	on	
12	5 %	isotropic	off	on	

Table Notes:

(1) Our model for radiation cooling involves no radiative transport, but rather assumes an optically transparent medium whereby energy is removed from the plasma in proportion to an average Planck opacity times the fourth power of the plasma temperature. As such, it represents an upper bound to local energy loss via radiative recombination.

(2) Self generated magnetic fields (sgmf) arise by conversion of thermal energy in the plasma to magnetic energy in regions where the pressure and density gradients are not parallel: i.e., near the edge of the laser beam. Self-generated magnetic fields are discussed in detail in Sections 4 and 5.

(3) The implicit model for thermal conduction was made more accurate for this simulation by limiting the timestep to 10^{-11} sec per computational cycle. This is the only difference between simulations 5 and 6. There is somewhat more thermal diffusion in model 6 than in the companion model 5.

(4) In all but model 9 above, our preionization of the ambient medium falls as $1/r^2$ from the laser focal spot and has the value quoted in the second column above at a point 1 cm from the laser focus. For model 9, the preionization still falls as $1/r^2$, but from points 1 cm distant from the center of the laser focus in the direction tangent to the target surface. This is perhaps the best that we can do with our 2 1/2 dimensional code in modeling a laser beam that misses the target, but interacts with the blast wave (and a preionized medium) that is produced by a second laser beam that does strike a solid target, traveling parallel to the first at a distance 1 cm from the first. This simulation could be compared to the NRL Pharos III experiment 86-590.

(5) Model 10 includes the $1/r^2$ model of preionization, but contains no target--clearly an unphysical situation. However, this model is of interest because it illustrates the behavior of the laser-induced cylindrical shock without its interaction with a spherical blast wave.

(6) The issue of the isotropy of thermal conduction is relevant only in the presence of a strong magnetic field (sufficiently strong so the product of the self-collision time and the gyro-frequency, which is linear in the magnetic induction, is greater than unity). Only models 11 and 12 contain magnetic fields of any kind, and these are thermally-generated from thermal energy in the plasma.

Figures 13 through 18 are snapshots of various physical quantities of interest in the models listed above at the time of 10 ns--2 ns after the laser pulse ends. To facilitate a comparison between the 12

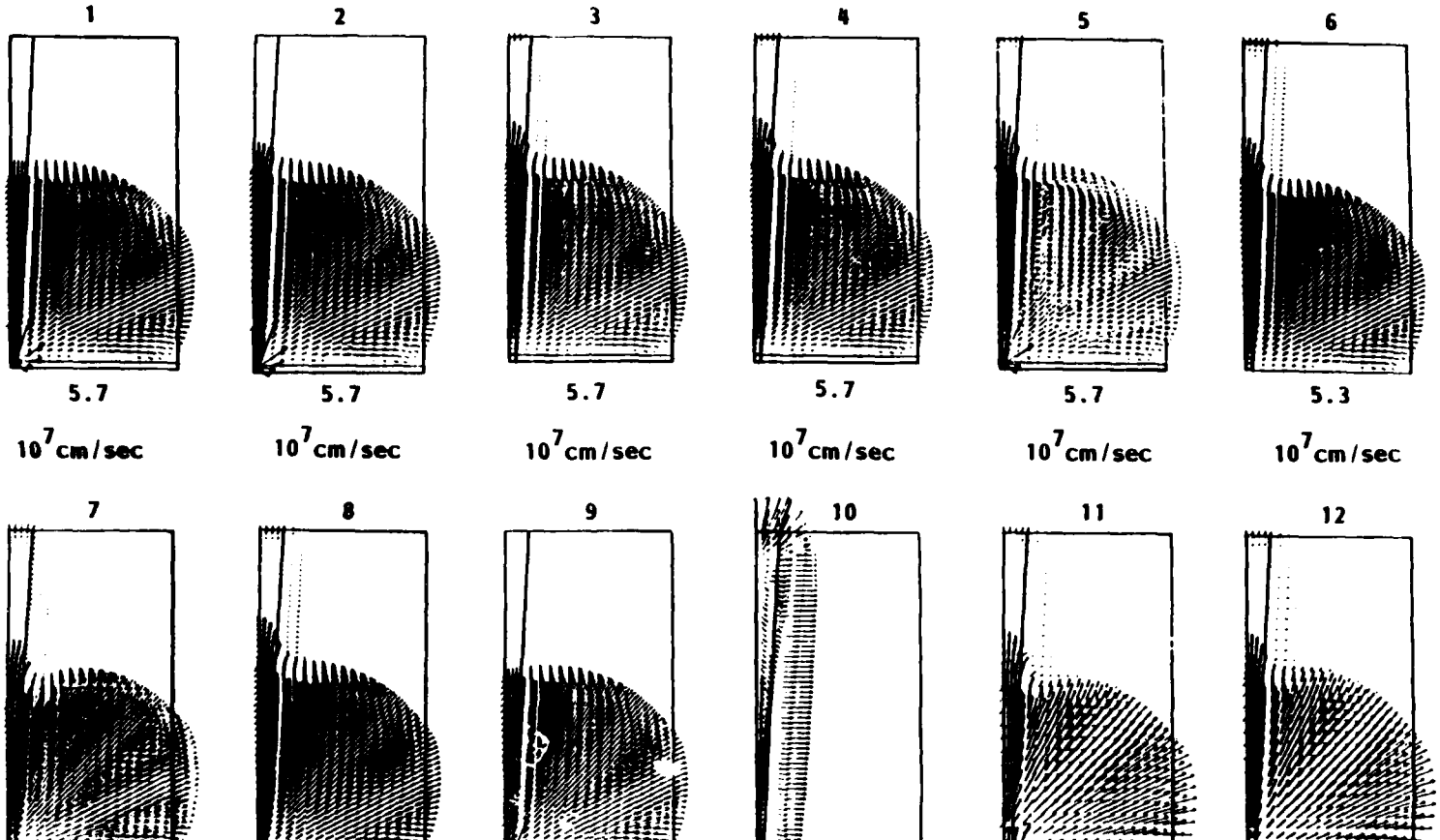

Figure 13. Velocity vectors for the 12 simulations discussed in Section 2.3.

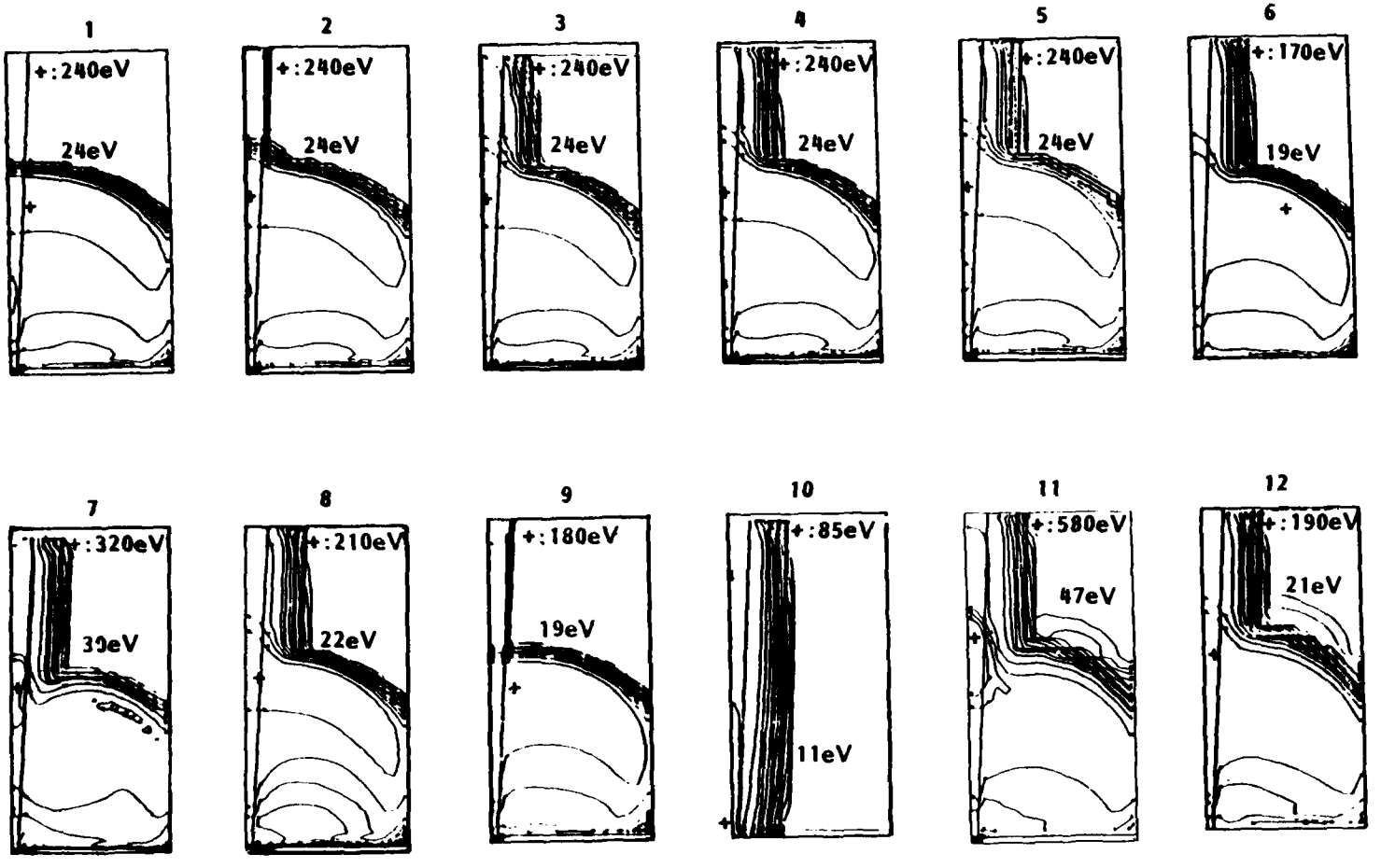

Figure 14. Temperature contours for the 12 simulations in Section 2.3. Plus (+) is the maximum value; below is noted the shell temperature.

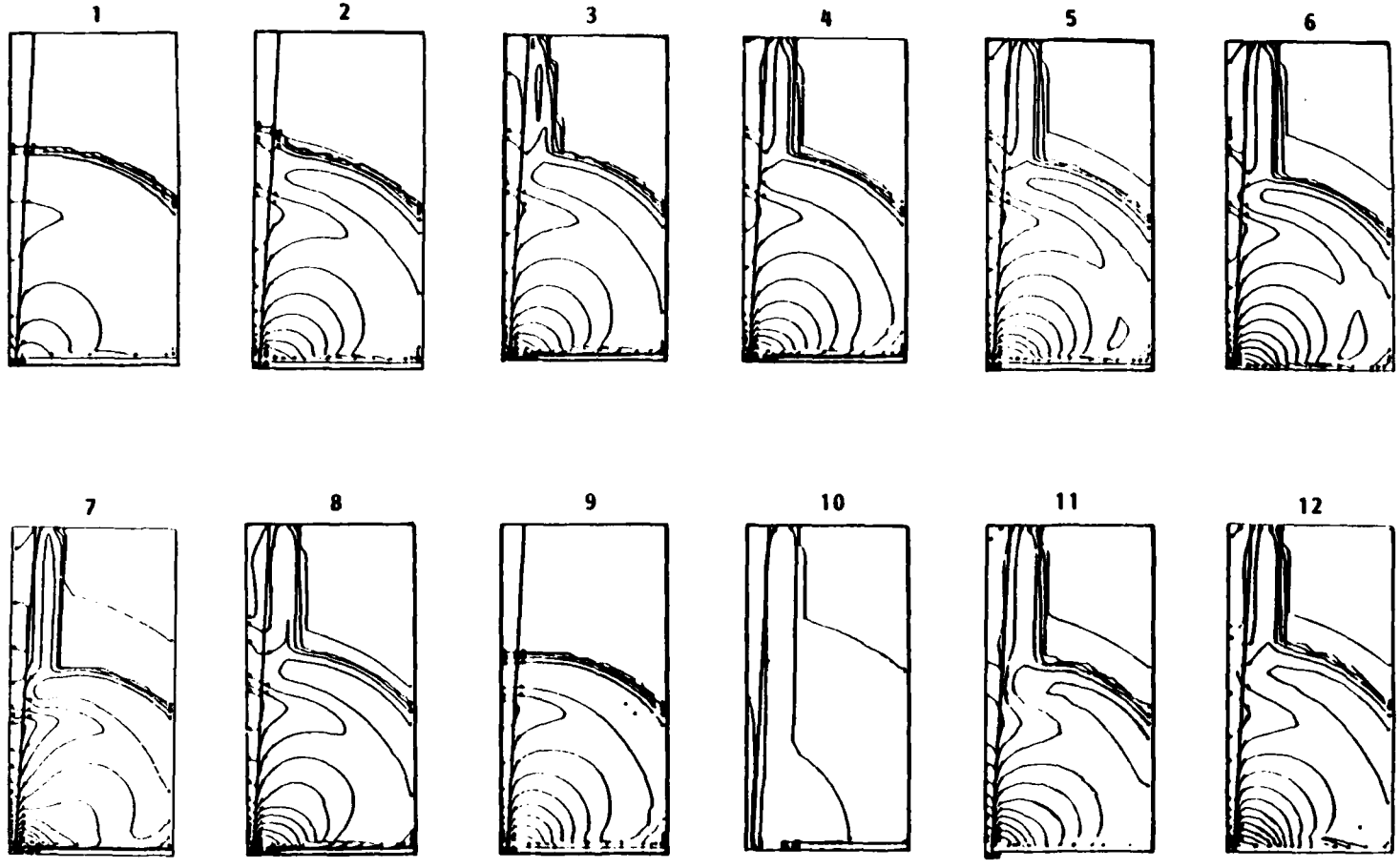

Figure 15. Electron number density contours for the 12 simulations in Section 2.3.

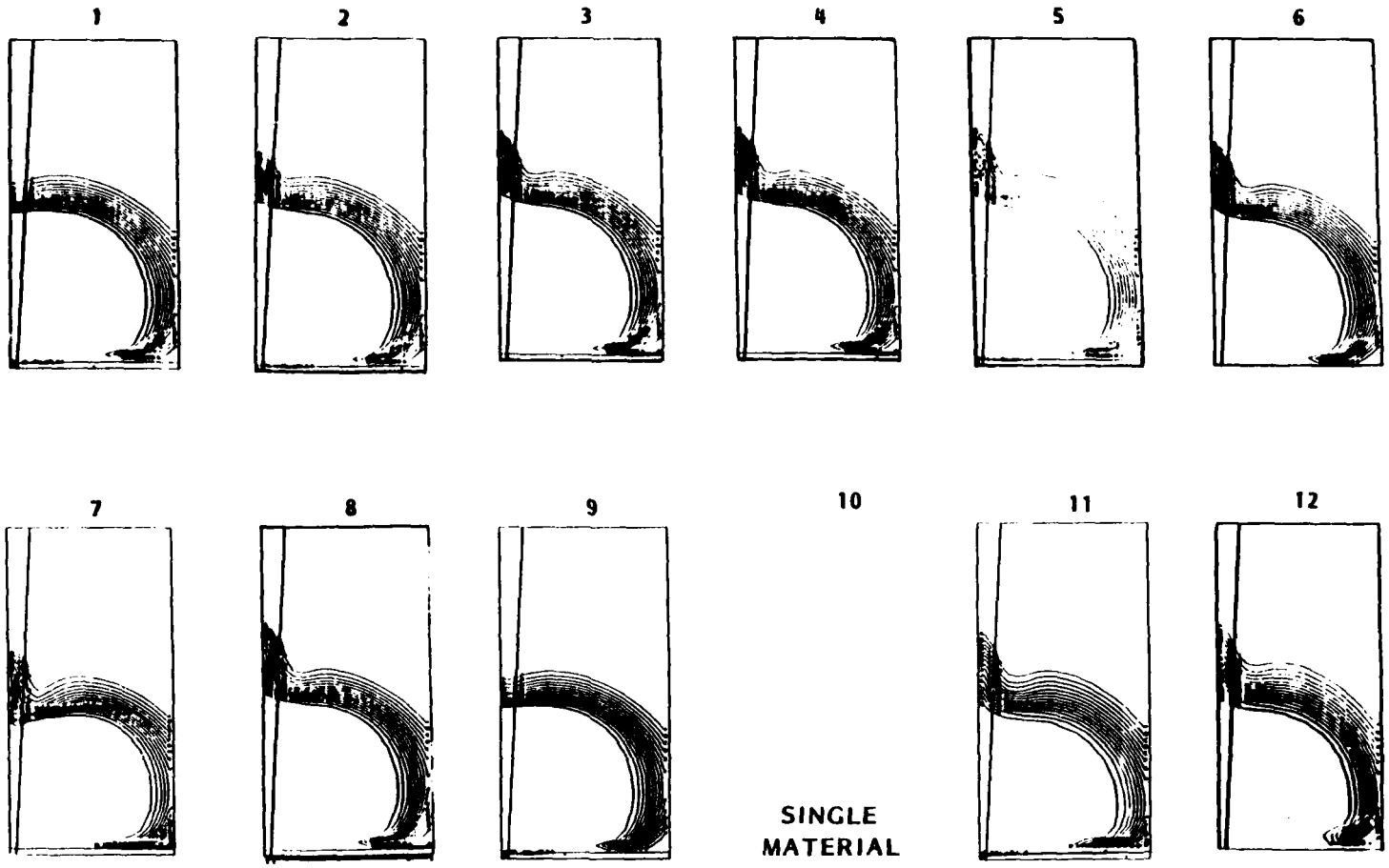

Figure 16. Material contours noting the approximate location of the debris-air interface for the 12 simulations in Section 2.3.

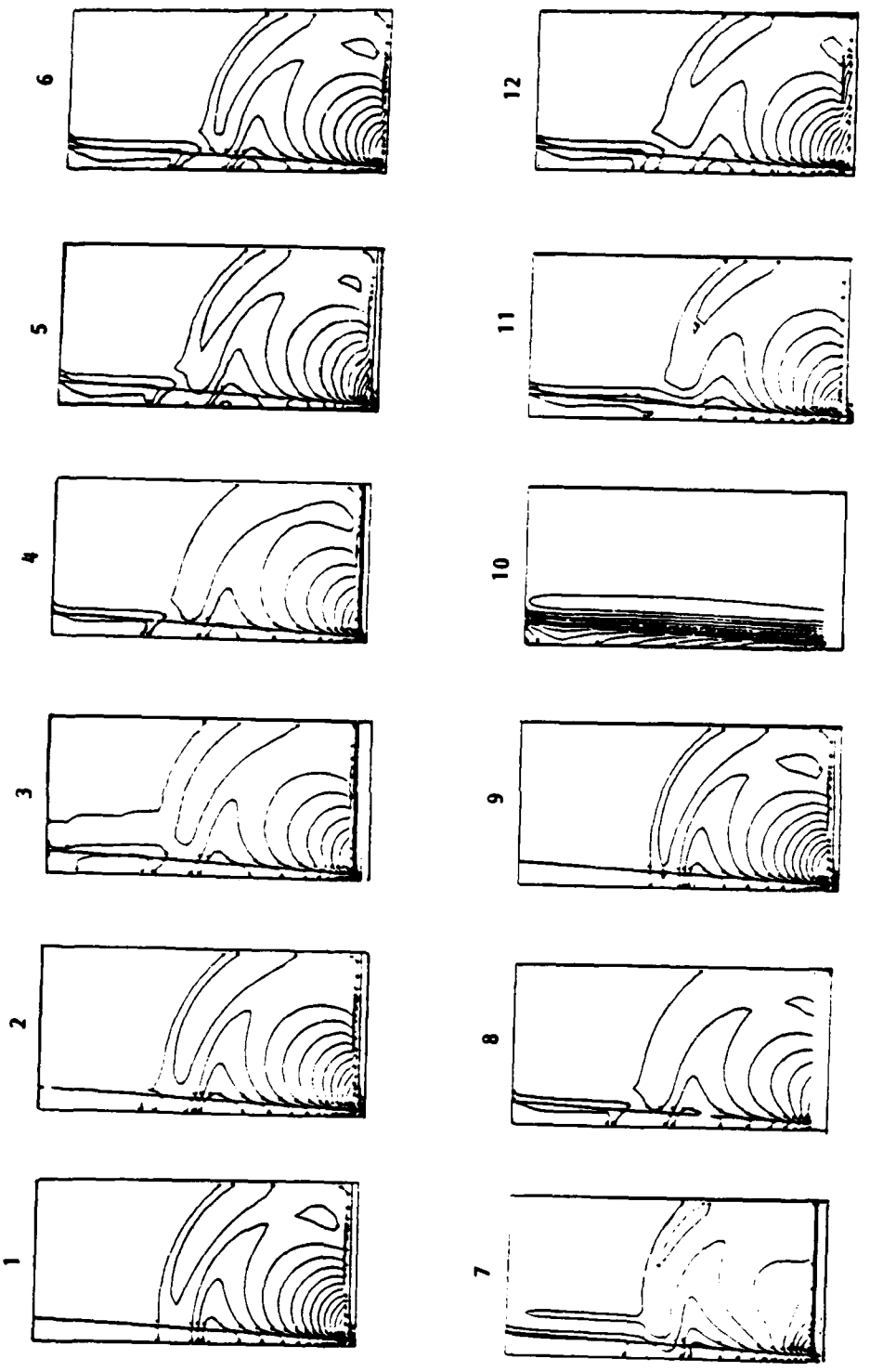

Figure 17. Mass density contours for the 12 simulations in Section 2.3.

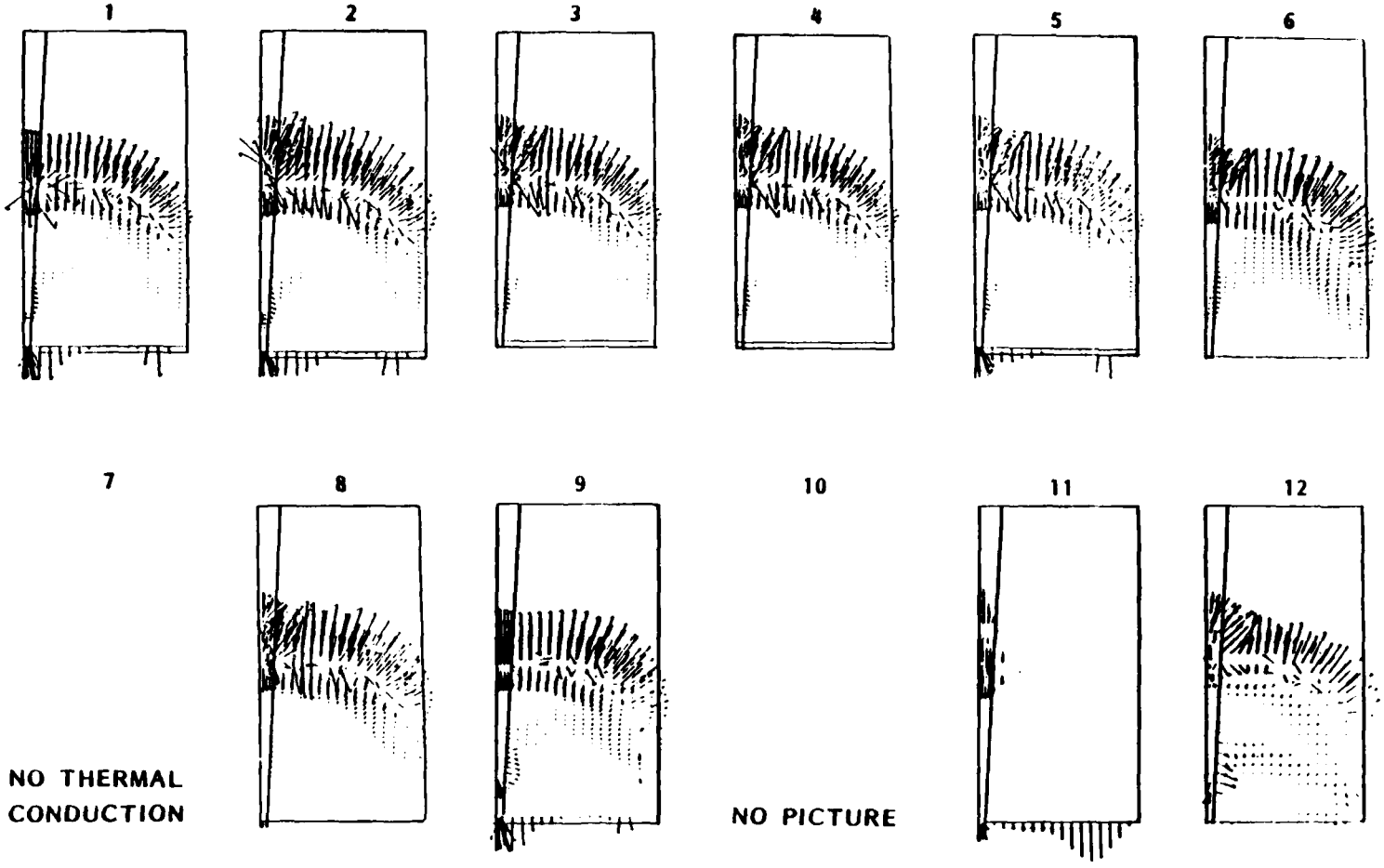

Figure 18. Thermal energy flux vectors for the 12 simulations in Section 2.3.

models, each figure contains 12 snapshots of a single physical attribute from the simulations--one from each model. Recall that the axis of symmetry is a vertical line on the left of each snapshot. The laser enters from above and is constrained to the channel that is marked by a line to the immediate right of the symmetry axis.

Figure 13 illustrates velocity vectors and the magnitude of the largest vector is noted below each snapshot. As we increase the degree of preionization in models 1 through 5, the size of the protrusion in the laser channel grows. This is the aneurysm, and the distance that it extends beyond the surrounding spherical blast front is sensitive to the degree of preionization. The maximum velocity in models 1 through 5 is the same: $5.7\ 10^7$ cm/sec. Model 6 is most similar to model 5; the accuracy of the implicit thermal diffusion model is somewhat better in model 6. The velocity snapshots look similar, but the maximum velocity is somewhat smaller in model 6 indicating that the increased thermal smoothing suppresses only the maximum plasma speed. Model 7 is 5 percent preionized, but has no thermal conduction. The peak velocity and the extent of the aneurysm are not as great as any of the models that are also 5 percent preionized but include thermal conduction. Model 8 radiates, but the effect of radiative cooling on the hydrodynamics seems from Figure 13 not to be great. Model 9 shows no aneurysm when the source of preionization is 1 cm off-axis. While not conclusive, this does indicate that experimentally one should not expect to see a laser-aligned aneurysm when the laser beam does not strike a target (as is the case in NRL shot 86-590). Model 10 contains no target, but includes the $1/r^2$ model for preionization that originates from the laser focal spot (an unphysical situation). The peak velocity profile indicates expansion from the heated channel. Models 11 and 12 include simulations of thermally-generated magnetic fields. The peak velocities in these two models are suppressed somewhat by the magnetic fields, but the relative position of the spherical blast front and the aneurysm are similar to model 5 that has the same value for the preionization.

Figure 14 illustrates iso-temperature contours on a logarithmic scale. The location of the maximum temperature is indicated by a plus (+) sign, and this peak value is noted at the top of each frame. An average temperature that is characteristic of the shell is noted also in each frame. The temperature contours in model 1 show a laser-heated channel not to be present, of course, as there is no preionization to seed laser absorption. A small dimple in the blast front appears in the laser channel at the smallest nonzero value of preionization in model 2. As the fractional preionization increases between models 2 and 5, the cylindrical laser-heated channel becomes more pronounced. Recall that it this laser-induced cylindrical structure that we interpret as the progenitor of the aneurysm. Interestingly, models 1 through 5 have the same model for thermal conduction, and all 5 models produce the same shell temperature and maximum temperature, independent of the fractional preionization. Model 6 is somewhat cooler than the first 5 models because that model encourages thermal diffusion. Model 7 has no thermal conduction and is about 20 percent hotter than models 1 through 5. However, the relative size of the cylindrical laser-heated channel and the spherical blast front is the same in models 5, 6, and 7. This strengthens our claim that thermal diffusion is not an important mechanism for aneurysm growth at this moderate value of the laser energy. Model 8 has the same model for thermal conduction as the first 5, but has our simple radiation cooling mechanism turned on. The cylindrical laser-heated channel persists, and the plasma temperature is about 10 percent smaller than the similar non-radiative models. Because the source of preionization is further away from the laser channel in model 9, the laser-heated channel is not as pronounced as in model 5. Model 10, without a target but with the same model of preionization and thermal conduction as model 5, shows a strong laser-induced cylindrical structure. Models 11 and 12 are 5 percent preionized just as model 5, but include thermally-generated magnetic fields. The structure of the laser-heated channel is similar for these 3 models. Notice, however, that model 11, with anisotropic thermal conduction, produces larger temperatures in the shell and in the bubble.

Figure 15 illustrates electron number density iso-contours on a logarithmic scale. The structure of these snapshots essentially mimics the corresponding temperature features of Figure 14.

Figure 16 illustrates the approximate position of the debris-air interface. The broadness of the band is a consequence of numerical diffusion of material across our Eulerian mesh. The middle of this band represents the location of the interface. This interface is essentially spherical outside the laser channel. Models 1 through 5 show that the debris-air interface protrudes ahead of the blast front at points within the channel by an amount proportional to the fractional preionization. This indicates that the aneurysm is made of target material. The laser-heated channel exists far in front of the aneurysm and consists of ambient material. Model 10 has no target, hence no debris.

Iso-density contours on a logarithmic scale are illustrated for our 12 models in Figure 17. They clearly illustrate the position of the spherical blast front and the laser-induced cylindrical blast wave. The mass density within the channel is less than the ambient channel, and this allows target debris to expand preferentially along the laser axis and create the aneurysm.

Finally, Figure 18 illustrates thermal flux vectors for 10 of the 12 models. Recall that model 7 does not compute thermal conduction. In all except model 11, the thermal flux is directed away from the hot shell in an essentially symmetric manner. However, in model 11, the thermal flux is seen mostly within the laser channel, and is suppressed outside the channel where thermally-generated magnetic fields are strong. These fields exist mostly within the shell away from the symmetry axis, and are toroidal in character. (Details are given in Section 5.) It is possible that for low energy laser pulses, where the preionization is not as great as we have assumed in these models, the anisotropic thermal conduction may anisotropize the blast wave.

2.4 CONCLUSIONS.

Simple analytic analysis suggests that the channel of ambient room temperature air through which the laser propagates can be heated to many eV via inverse bremsstrahlung laser absorption by that air if it has a non-zero ionization fraction. The change in temperature of the ambient gas is proportional to the ionization fraction of the gas (Equation 7). Therefore, there must exist some mechanism for preionizing the room temperature ambient medium in order to initiate laser absorption. There is some experimental evidence that the ambient medium is preionized by a few percent at a distance of 1 cm from the target surface, perhaps due to X-rays emanating from the laser-irradiated target and other hot plasma. This degree of preionization is sufficient to initiate heating of the channel material by the laser.

MACH2 simulations give conclusive evidence that a laser-heated channel leads to the formation of a central aneurysm in NRL laser/HANE experiments. The seed for the formation of an aneurysm appears by the time of peak laser power as a weak cylindrical shock centered about the laser axis. If the heating is appreciable far from the target on a time scale comparable to the length of the laser pulse, an aneurysm will be evident at later times. Heating in the laser channel is proportional to the ionization fraction, as well as to the laser intensity, so the aneurysm may scale with laser energy (this is consistent with shadowgraphs from low energy shots). Figure 8, a superposition of the electron number density generated by MACH2 for a simulation that is five percent preionized 1 cm from the target surface upon a digitization of an NRL shadowgraph from experimental shot number 85-544 illustrates excellent agreement between experiment and theory. Figure 11, a superposition of an early-time shadowgraph from NRL experiment 86-625 and a picture from a computer simulation of that shot at the same time, shows the laser-induced cylindrical shock front from the experiment and a computer simulation of the same.

SECTION 3

A SIMPLE MODEL FOR LASER CHANNEL-HEATING IN FEW-TORR PLASMA

A hot, low density laser channel has been shown to be important in many of the simulations discussed in this report. The cylindrical blast from the heating is seen in the shadowgraphs at early-time (10 ns), and we has shown that it is the primary cause of the on-axis aneurysm seen in the NRL experiments. Because of this direct cause-and-effect relationship, it is of interest to inquire how the laser heating depends on the experimental parameters. Since this heating takes place during the laser pulse (1 - 6 ns), it is reasonable to ignore the hydrodynamics and other slower processes, and consider the extent and nature of the initial heated region as a separate problem. In this section we develop a simple model of the heated channel that agrees very well with the detailed two-dimensional models, and allows computation of scaling laws for the heating process. We will thus demonstrate that direct inverse-bremsstrahlung deposition of laser energy can account for the observed and computed features of the channel, and that no shock or detonation mechanisms appear to be operating in this regime during the laser pulse. The model used here is a direct extension of that of Section 2.1, used to motivate the channel-heating simulations.

The incident laser energy propagates through the underdense ambient medium and deposits the bulk of its energy at the critical surface, which is the target surface at the onset of the laser pulse. Experimental evidence indicates that a brief burst of X rays are emitted from the target during the early stages of the laser pulse. These X rays photoionize the ambient gas (bound-free absorption) and provide the seeds for inverse bremsstrahlungen (free-free) absorption of the incident laser beam by the ambient gas. We do not attempt to model this initial target heating and photoionization process here, but instead simply assume that the ambient

gas is initially ionized with an ionization fraction that drops as $1/r^2$ where r is the distance from the target. The degree of ionization is found experimentally to be in the range of one--few percent at a distance of 1 cm from the target.

The laser intensity in the channel is given by $I = I_0 \exp(-\int K\, dr)$, or, for small absorption, $I = I_0 (1-\int K\, dr)$, where I_0 is the incident intensity, and K is the absorption coefficient (units of m^{-1}). The formula for the inverse bremsstrahlung absorption coefficient has been given by Johnston and Dawson, 1973 (Ref. 17). For the present case (electron density much less than critical), this coefficient is given by Equation (3) and is repeated for clarity:

$$\kappa_\nu = \beta b \lambda^2 \frac{\zeta' \zeta^2 \rho^2 \ln \Lambda}{A^2 T^{3/2}} \qquad (16)$$

where λ is the laser wavelength, $\ln(\Lambda)$ is the coulomb logarithm (varies from 1 - 5 for these cases), ζ is the number of free electrons per nucleon, $\zeta' = \max(\zeta, 1)$, A is the atomic number of the gas, ρ the density of the gas, and T the local gas temperature. The product βb is $1.5666 \times 10^{18}/m$ for mks units with T in eV. The important point here is that the absorption depends strongly on ionization state and inversely on the ambient temperature. The ζ' factor accounts for the presence of neutral ambient atoms at low degrees of ionization.

The time derivative of temperature at a point in the channel is given by:

$$\frac{dT}{dt} = \frac{\kappa_\nu I}{\rho C_v} \qquad , \qquad (17)$$

where κ_ν is given by Equation (16), I is the local laser intensity, and C_v is the specific heat. The intensity will depend on the time variation of the laser energy as well as the distance from the target. For a perfect gas, $C_v = 1.44 \times 10^8 \ (1 + \zeta)/A$ J/eV-kg.

We may integrate Equation (17) directly to obtain an estimate of the final temperature of the laser-heated channel. We assume fully ionized nitrogen as the ambient gas, ρ = 5 Torr, λ = 1 micron, $\ln(\Lambda) = 3$, and find

$$T_f \approx (6\ E/r^2)^{2/5} \quad , \tag{13}$$

where E is the laser energy in Joules, and r is the local channel radius in centimeters, T_f the final temperature in eV, and we have assumed that the initial channel temperature is small. Given these assumptions, Equation (18) in consistant with Equation (7). Taking E_l = 100 J, and r = 0.05 cm, we find T_f = 142 eV, so a hot channel is expected and should extend a considerable distance along the laser channel, since the dependence on distance is weak. On the other hand, the final temperature is approximately linearly dependent upon the degree of ionization, producing a feedback mechanism that should shut off the heating at a distance where the available deposited energy is too small to ionize the ambient gas.

A better estimate of the channel temperature as a function of time (during the laser pulse) and distance from the target is obtained by numerical integration of Equation (17) with time dependent quantities included. For this estimate a Gaussian pulse shape is used for the laser power, peaking at 4 ns, ending at 8 ns, the position in the channel determines the level of preionization and the channel radius, the Coulomb logarithm is given by (Spitzer, 1962, Ref. 18):

$$\ln(\Lambda) = \ln(\min (4.9e9\ T^{1.5}\ \lambda/\zeta,\ 8.08e8\ T\ \lambda)) \tag{14}$$

with $\ln(\Lambda) >= 1$.

The ionization fraction, ζ, is given by a fit to Saha equilibrium at 5 Torr pressure of atomic nitrogen shown in Figure 19. At this pressure nitrogen begins to ionize at about 1 eV, is five times ionized at 10 - 30 eV, and is fully ionized at 90 eV.

The specific heat, C_v, for nitrogen is shown in Figure 20. The irregular line is taken from a tabular equation of state for nitrogen at 5 Torr pressure, the line labeled "fit" is the rough fit used for the present models, and the dashed line is the perfect gas value ignoring ionization energy. By comparing the areas above and below the dashed line, we conclude that for temperatures in the 0.1 - 100 eV range most of the laser energy absorbed in the channel is needed to ionize the gas.

We have integrated Equation (17) for target distances ranging from 0.1 to 3 cm. We call the result of these integrations the "zero dimensional" (or 0 D) model, since each point in the channel is heated completely independently of all other points. The results depend on the degree of preionization of the channel. Figure 21 shows the case of 5 percent ionized at 1 cm from the target. Temperatures are shown as a function of distance along the channel for times of 0 (room temperature) to 8 ns (end of laser pulse). The result from Equation (18) is labeled "simple estimate." As expected, Equation (18) is a good estimate of channel heating for regions that become fully ionized (0 - 0.5 cm), but beyond 0.5 cm the temperature in the channel drops, with little heating beyond 0.9 cm. An ionization front moves to larger radii in this figure with a mean velocity of about 10^8 cm/s, heating the gas from ambient temperatures to about 100 eV, but it is not a progressive wave, since no coupling between different radii is included in the model.

The result is a channel heated to about 100 eV extending from the target to about 0.9 cm along the channel. This heated region expands hydrodynamically as a cylindrical shock wave and forms a low density channel at later times. The spherical blast wave expands more rapidly in this channel, resulting in aneurism formation. When the blast wave moves beyond the heated region, the aneurism should decay.

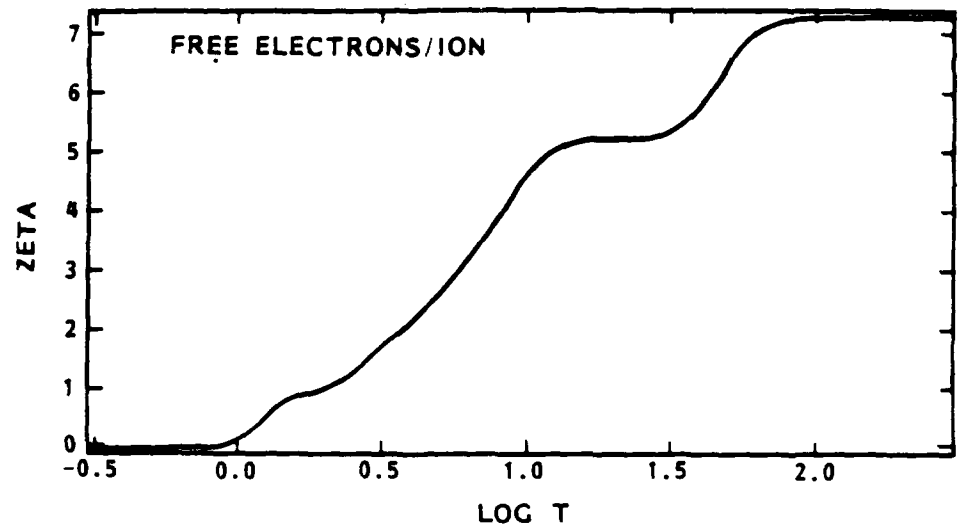

Figure 19. Fit to tabular equation of state for the ionization fraction of nitrogen at 5 Torr pressure as a function of temperature. These numbers agree with Saha equilibrium values.

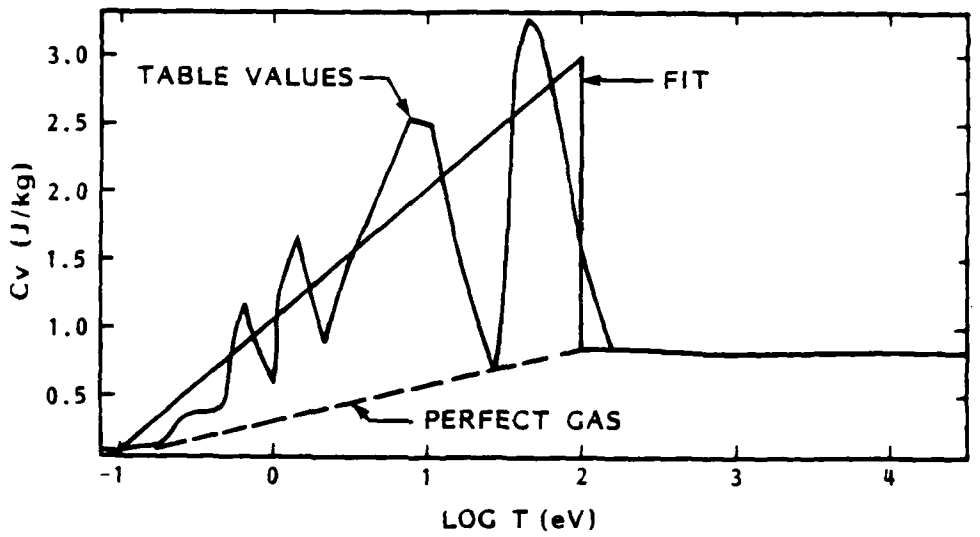

Figure 20. Fit to tabular equation of state for the specific heat of nitrogen at 5 Torr pressure as a function of temperature. Both the exact tabular values (irregular solid line) and the simple approximation used here are shown. The dashed line is an estimate of the perfect gas value obtained when ionization energy is ignored.

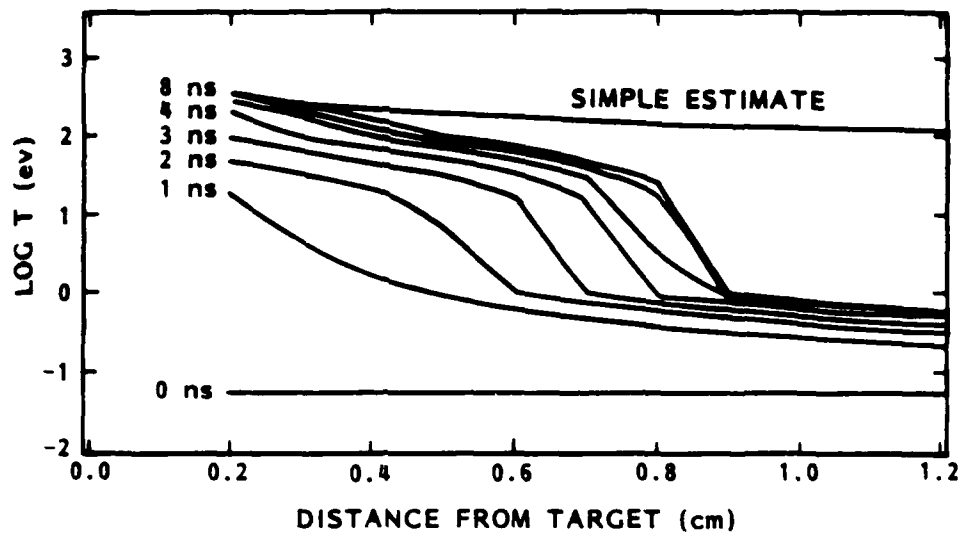

Figure 21. Run of temperature versus position in the channel at various times during the laser pulse for case 1 of Table 2. Also shown is the result obtained from Equation (18) labeled "simple estimate".

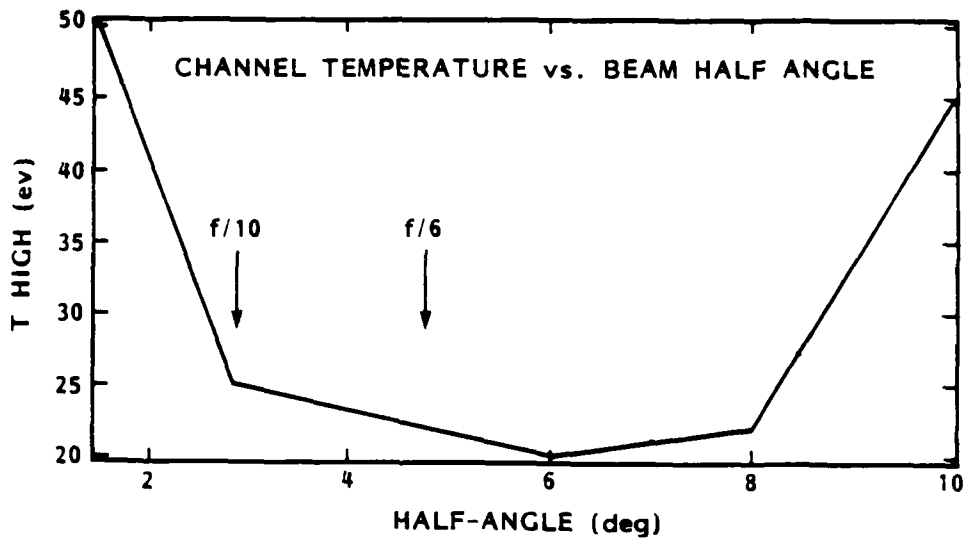

Figure 22. Temperature at the head of the heated channel as a function of the convergence angle of the laser beam. The two laser configurations used at NRL are shown.

Table 2 shows the results of a number of models run with various values for the laser energy (E), ambient pressure (P), and degree of preionization at 1 cm (ζ_0). The listed parameters are: L = extent of heated region from target of preionization of the ambient gas (cm), T_{high} = temperature at the top of the ionization wave (eV), T_{low} = temperature at the bottom of the ionization wave (distance = size)(eV).

Table 2. Laser heated channel characteristics.

	E	λ	P	ζ_0	angle	L	T_{high}	T_{low}
1	109	1.0	5.0	5.0	2.86	0.9	25	1.0
2	109	1.0	5.0	2.5	2.86	0.7	45	1.0
3	109	1.0	5.0	10.0	2.86	1.1	20	1.0
4	109	1.0	2.5	5.0	2.86	0.8	16	1.0
5	109	1.0	10.0	5.0	2.86	1.0	40	1.0
6	50	1.0	5.0	5.0	2.86	0.8	16	1.0
7	200	1.0	5.0	5.0	2.86	1.0	30	1.0
8	109	1.0	5.0	5.0	10.0	0.6	45	1.0
9	109	1.0	5.0	5.0	8.0	0.65	22	1.0
10	109	1.0	5.0	5.0	6.0	0.7	20	1.0
11	109	1.0	5.0	5.0	1.5	1.1	50	1.0
12	109	1.0	5.0	5.0	0.0	2.5	400	1.0
13	109	0.5	5.0	5.0	2.86	0.7	20	1.0
14	109	2.0	5.0	5.9	2.86	1.2	100	1.0

The size of the heated region in models 1 - 7 is fit to an accuracy of 2 percent by the scaling law:

$$L = 0.19\, E^{0.16}\, P^{0.16}\, \zeta_0^{0.33} \quad , \tag{20}$$

where L is the length of the heated region in centimeters, P is the ambient pressure of N_2, and ζ_0 is the percent preionization at 1 cm from the target. For example, for ζ_0 = 5%, E = 100 J, and P = 5 Torr, we find L = 0.89 cm.

The scaling law for a simple blast wave (Equation (14)) is:

$$R = 0.123\ (E/P)^{0.2}\ t^{0.4} \quad . \tag{21}$$

The energy scaling of Equation (20) is that of a normal blast wave, but the pressure scaling is the opposite of the blast wave case. This means that, as the ambient pressure is increased, the size of the aneurism produced increases while the position of the blast wave at a fixed time decreases, causing the pressure dependence to be the most obvious in the experiments. Increasing the laser energy causes both the heated channel and the blast wave position to increase similarly, so the size of the aneurism appears to be independent of this quantity.

The results from Table 2 for the temperature at the head of the ionization wave are fit to 10 percent accuracy by the scaling law:

$$T_{high} = 2.45\ E^{0.48}\ P^{0.66}\ \zeta_0^{-0.58} \quad . \tag{22}$$

The temperature increases with laser energy and ambient pressure, but decreases strongly as the preionization is increased. The effect of varying the preionization is simply to change L while maintaining the temperature as a function of distance nearly unchanged, thus producing higher "head" temperatures for the shorter channels.

The models 8 - 12 in Table 2 show the dependence upon the convergence angle of the laser beam. We see that for longer focal length lasers the size of the aneurysm is much longer, while the temperature increases for both small and large beam angles. This probably explains why the aneurysm became much more obvious when the laser at NRL was upgraded to a higher energy configuration and the focal length was changed from a f/6 (4.75 degree half-angle) to a f/10 (2.86 degree half-angle) focal ratio. The dependence of size (L) on half-angle of the beam is given approximately by

$$L = 1.26\ (\text{half-angle})^{-0.32} \quad , \tag{23}$$

where the angle is in degrees and L is in cm. The dependence of temperature upon angle is shown in Figure 22. In both Equation (23) and Figure 22 the zero angle model has been omitted, and should be regarded as a limiting case.

We now consider the details of the absorption process. Figure 23 shows the absorption coefficient, κ_ν (Equation (16)) versus distance for model 1 in Table 2 at times 1 - 8 ns. At very early times the absorption occurs near the target, but as early as 2 ns the peak absorption has moved away from the target and henceforth occurs near the head of the channel where the number of free electrons is high and the temperature is still relatively low. Absorption near the target is very low at later times due to the very high temperatures in this region. Integrating these curves, we obtain the total fraction absorption versus time curve shown in Figure 24. The absorption increases during the first half of the laser pulse (0 - 4 ns), then levels out at about 0.5 percent. This results in about 0.5 J energy absorbed in the channel for a 100 J laser pulse, in agreement with the two-dimensional models.

Finally, models 13 and 14 show the effect of varying the laser wavelength. The size of the heated region is given to an accuracy of 1 percent by

$$L = 0.91\ \lambda^{0.39} \quad , \tag{24}$$

where L is in cm and λ is in microns. The temperature of the plume is relatively constant below λ = 1 micron, and increases rapidly for longer wavelengths to 100 eV at 2 microns and several keV at 10 microns (not shown).

This model makes no allowance for a variety of possible cooling mechanisms, and thus represents an upper limit estimate of the channel heating. In the first 3 ns of target irradiation, however, there is no

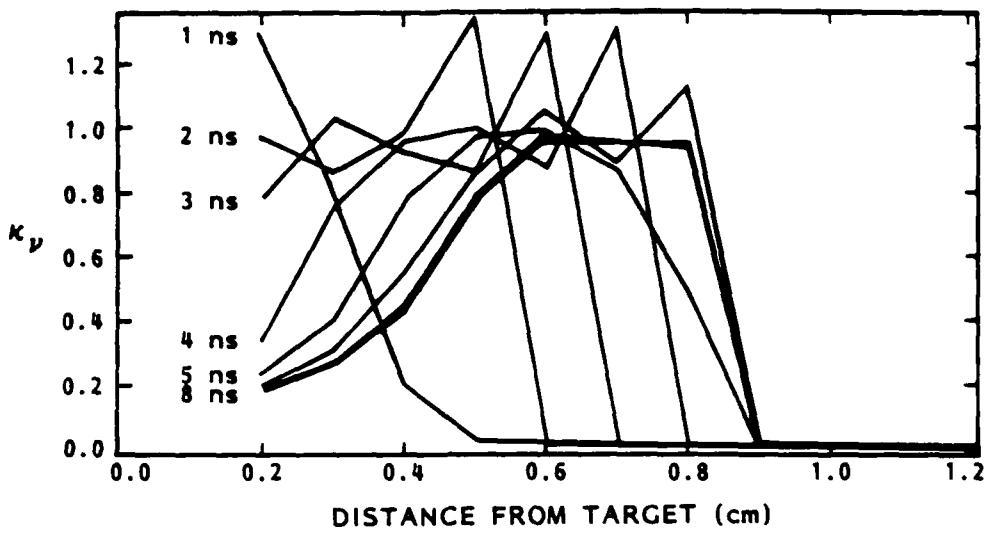

Figure 23. Absorption coefficient (Equation (16)) versus position in the channel at various times during the laser pulse for model 1 of Table 2.

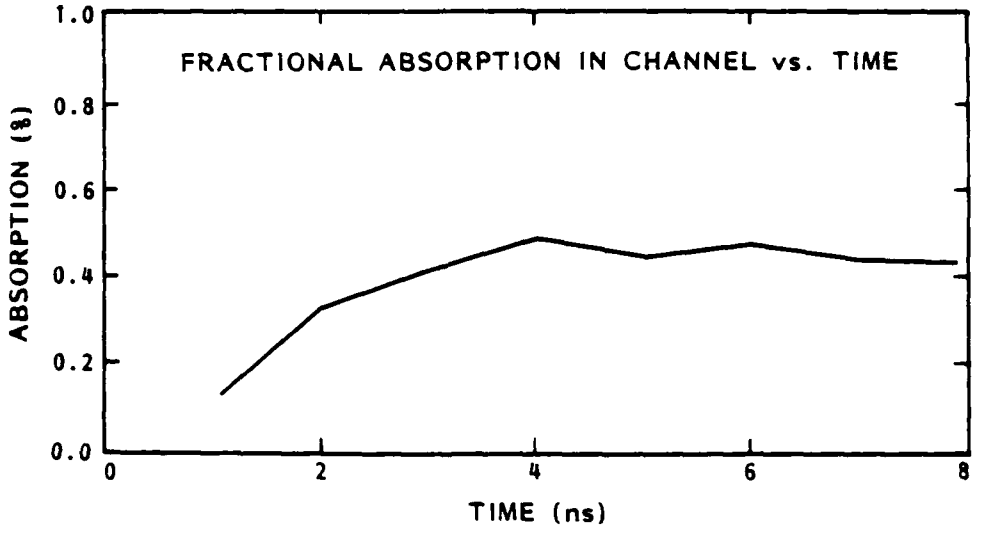

Figure 24. Instantaneous fractional absorption as a function of time during the laser pulse for model 1 of Table 2. Peak laser power occurs at 4 ns.

time for hydrodynamic expansion, thermal conduction, or radiation cooling, so these estimates should be quite reasonable. In fact, the two-dimensional simulations show almost identical temperature profiles to those shown here, proving that this model is an accurate representation of the laser channel heating.

SECTION 4

CAN THERMALLY GENERATED MAGNETIC FIELDS BE INCORPORATED INTO A SINGLE FLUID MODEL?

4.1 INTRODUCTION.

This section addresses the question of whether it is reasonable to include the process known as thermally (or self) generated magnetic fields into a single fluid magnetohydrodynamics (MHD) model. Our conclusion is that it is indeed possible to model this effect in this way. An outline of the path along which we travel to arrive at this conclusion follows. We then, in the following section, illustrate the thermal generation of magnetic fields with a two-dimensional MHD code, MACH2.

4.2 THEORY FOR EACH PLASMA SPECIES.

We begin with the fluid equations for charged particles of species s. The species are either ions (s = i) or electrons (s = e), each of which is characterized by a mass, m_s and charge, q_s. The momenta of the particles are assumed to be influenced only by electric and magnetic fields, $\vec{E}$ and $\vec{B}$, and by collisions. The equation of motion for an ensemble of particles of species, s, with a number density, $n_s(\vec{r},t)$, follows from the Vlasov equation if we assume a suitably smooth thermal spread in the velocity distribution:

$$m_s n_s \frac{d\vec{v}_s}{dt} - q_s n_s \left[\vec{E} + \frac{\vec{v}_s}{c} \times \vec{B} \right] + \nabla P_s - \vec{K}_s = 0 \quad . \tag{25}$$

We will employ cgs units throughout this section. The fluid velocity, $\vec{v}_s$, is an ensemble average of single particle velocities. The pressure, P_s, is related to the temperature by an equation of state. The temperature is simply a measure of the mean square thermal speed, v_s^2, for particles of mass, m_s. The final term in Equation (25) is a source of momentum per unit volume that is caused by inter-species collisions. Let us assume $\vec{K}_e = -\vec{K}_i$ for a nonviscous fluid.

The fluid of each species obeys a continuity equation

$$\frac{\partial}{\partial t}(n_s) + \nabla_j(n_s v_s^j) = 0 \quad , \tag{26}$$

if the total number of particles of each species is conserved. We employ the summation convention whereby a sum from 1 to 3 over repeated indices is implied.

4.3 MHD EQUATIONS.

A single fluid comprised of electrons and ions may be characterized by its total mass density, momentum density, current density, charge density, and thermal energy density (pressure). Each is defined as the sum of the contributions from each species. Therefore, with the convention $e = 4.803\ 10^{-10}$ esu, the charge of each free electron is $q_e = -e$ and the charge on the average ion is $q = +\zeta e$. ζ is between 0 and the atomic number of the ion species. Because we allow ζ less than unity, we may include neutral atoms among our ions. Hence:

mass density: $$\rho(\vec{r}) = m_i n_i(\vec{r}) + m_e n_e(\vec{r}) \tag{27}$$

charge density: $$\rho_c(\vec{r}) = e(\zeta n_i(\vec{r}) - n_e(\vec{r})) \tag{28}$$

momentum density: $$\rho\vec{v} = m_i n_i(\vec{r})\vec{v}_i(\vec{r}) + m_e n_e(\vec{r})\vec{v}_e(\vec{r}) \tag{29}$$

current density: $$\vec{J} = e(\zeta n_i(\vec{r})\vec{v}_i(\vec{r}) - n_e(\vec{r})\vec{v}_e(\vec{r})) \tag{30}$$

Pressure: $$P = P_i + P_e \quad . \tag{31}$$

By combining the continuity equations and the equation of motion for each species with the above definitions, one may derive single-fluid equations. For example, by summing over both species the product of the continuity equation and the mass for each species, one obtains the mass conservation equation:

$$\frac{\partial \rho}{\partial t} + \nabla_j (\rho v^j) = 0 \tag{32}$$

To obtain a single-fluid equation of motion, it is desirable to express the velocity for each species in terms of the center of mass velocity, $\vec{v}$, and the net current, $\vec{J}$. One obtains:

$$\vec{v}_i = \left(1 + \frac{m_e n_e}{m_i n_i}\right)\left(1 + \frac{m_e}{m_i}\zeta\right)^{-1} \vec{v} + \frac{\vec{J} m_e}{e\rho} \quad . \tag{33}$$

and

$$\vec{v}_e = \left(1 + \frac{m_e}{m_i}\zeta\right)^{-1} \left[\zeta \frac{\rho \vec{v}}{n_e m_i} - \frac{\vec{J}}{e n_e}\right] \quad . \tag{34}$$

In order to proceed further, we assume quasi-neutrality: $\rho_c \approx 0$. In this case, the electron number density, n_e, is related to the ion number density via Equation (28); i.e., $n_e = \zeta n_i$. Hence

$$\vec{v}_i \approx \vec{v} + \frac{\vec{J}}{e} \frac{m_e}{\rho} \tag{35}$$

and

$$\vec{v}_e \approx \vec{v} - \frac{\vec{J}}{e} \frac{m_i}{\rho\zeta} \quad . \tag{36}$$

Note that the difference between the velocities of the two species is parallel to the current density,

$$\vec{v}_i - \vec{v}_e \approx \frac{\vec{J}}{en_e} \quad , \tag{37}$$

and the sum is,

$$\vec{v}_i + \vec{v}_e \approx 2\vec{v} - \frac{\vec{J}m_i}{e\rho\zeta}\left(1 - \zeta\frac{m_e}{m_i}\right) \quad . \tag{38}$$

neglecting $\zeta\, m_e/m_i$ compared to unity, and using Equation (36), we find that $\vec{v}_i \approx \vec{v}$.

In going from the particle description to a fluid model, we replace the eight particle variables $\vec{v}_i$, $\vec{v}_e$, n_i, n_e with the eight fluid variables, $\vec{v}$, $\vec{J}$, ρ, ρ_c. In MHD, we restrict our attention to quasi-neutral fluids with $\rho_c = 0$. An additional assumption is that of ion-electron equilibrium, in which case the electron temperature is equal to the ion temperature, $T_e = T_i$. In this case, $P_e = \zeta P_i$, and as the total pressure is simply $P_e + P_i$, we have $P_e = (\zeta/1+\zeta)\ P$ and $P_i = (1/1+\zeta)\ P$.

By adding and subtracting the two particle equations of motion Equation (25), we obtain a fluid equation of motion and a generalized Ohm's law.

Under the assumptions of quasi-neutrality and electron-ion equilibrium, we obtain

$$\rho\frac{d\vec{v}}{dt} = \frac{\vec{J}}{c} \times \vec{B} - \nabla P \tag{39}$$

as the equation of motion for a quasi-neutral conducting fluid. If fluid viscosity is included in our model, we must add to Equation (39) the term $\nabla \cdot \vec{\vec{\sigma}}$ where $\vec{\vec{\sigma}}$ is a viscous dyad. Under these same assumptions, neglecting terms of order m_e/m_i when compared to unity, we have

$$\frac{d}{dt}\left(\frac{\vec{J}}{n_e}\right) = \frac{e^2}{m_e}\left(\vec{E} + \frac{\vec{v}}{c} \times \vec{B}\right) - \frac{e}{m_e n_e c}\vec{J} \times \vec{B}$$

$$+ \frac{e}{(1+\zeta)m_e n_i}\nabla P + \frac{e}{m_e n_e}\vec{K} \quad , \tag{40}$$

to lowest order as a generalized Ohm's law. The various current generating terms on the right hand side of Equation (40) are the electric field, $\vec{E}$, the electromotive induction, $(\vec{v}/c \times \vec{B})$, the Hall effect, $(\vec{J} \times \vec{B})$, the electron pressure, ∇P, and a collisional source term, $\vec{K}$. This source term will be considered to arise solely from interspecies collisions, and hence can be identified with the familiar resistive term

$$\vec{K} = -\frac{en_e}{\sigma}\vec{J} \tag{41}$$

where σ is the electrical conductivity of the fluid. Other sources of momentum for the particles such as radiation pressure or a thermoelectric force are not considered here. We may use the mass conservation Equation (32) to express the left hand side of Equation (40), the electron inertia term, as

$$\frac{d}{dt}\left(\frac{\vec{J}}{n_e}\right) = \frac{1}{n_e}\left[\frac{d\vec{J}}{dt} + \vec{J}\,(\nabla\cdot\vec{v})\right] \quad . \tag{42}$$

The electric and magnetic fields, and the current density, are related via Maxwell's equations. By solving Equation (40) for the electric field and taking its curl, we obtain from Faraday's law an equation for the time derivative of the magnetic field. We express the current density in terms of the curl of the magnetic field (Ampere's law) by neglecting the displacement current. Such neglect is consistent with our assumption of quasi-neutrality whereby the charge density is approximately zero, as is it's partial derivative with respect to time. After performing some algebra, we obtain the equation for magnetic field generation:

$$\frac{\partial \vec{B}}{\partial t} = \nabla \times (\vec{v} \times \vec{B}) + \frac{c^2}{4\pi\sigma}\left[\nabla^2\vec{B} + \left(\frac{\nabla\sigma}{\sigma}\right) \times (\nabla \times \vec{B})\right]$$
$$- \frac{c}{e(1+\zeta)n_i}\left\{\frac{\nabla[(1+\zeta)n_i]}{(1+\zeta)n_i}\right\} \times \nabla P$$
$$+ \frac{c}{4\pi n_e e}\left[\left(\frac{\nabla n_e}{n_e}\right) \times (\vec{B}\cdot\nabla\vec{B} - \frac{1}{2}\nabla B^2) - \nabla \times (\vec{B}\cdot\nabla\vec{B})\right] \qquad (43)$$
$$+ \frac{m_e c}{n_e e^2}\left[\left(\frac{\nabla n_e}{n_e}\right) \times \left(\frac{d\vec{J}}{dt} + \vec{J}\,(\nabla\cdot\vec{v})\right) - \frac{d}{dt}(\nabla \times \vec{J}) - (\nabla \times \vec{J})\,(\nabla\cdot\vec{v})\right].$$

The current density occurring in the last term can be replaced with $c/4\pi\ \nabla \times \vec{B}$, and the curl of $\vec{J}$ with $-c/4\pi\ \nabla^2 B$.

Note that if the gradient of the number density, the velocity, and the gradient of the conductivity all vanish, and if we can ignore the $d(\nabla \times \vec{J})/dt$ term, we recover the familiar diffusion equation for the magnetic field:

$$\frac{\partial \vec{B}}{\partial t} = \frac{c^2}{4\pi\sigma}\nabla^2\vec{B} \quad . \qquad (44)$$

In general, however, all of the terms of Equation (43) contribute to the generation of $\vec{B}$, although the contribution from higher-order terms may be small in some cases.

Under certain circumstances, the electron inertia and the Hall terms from Equation (39) may be small. In this case,

$$\vec{E} = \frac{1}{\sigma}\vec{J} - \frac{\vec{v}}{c} \times \vec{B} - \frac{1}{e(1+\zeta)n_i}\nabla P \quad . \qquad (45)$$

The last term in the above equation is an effective electric field in the direction of the fluid pressure gradient--similar to the thermoelectric effect. The curl of this last term generates a magnetic induction in the direction of $\nabla n_e \times \nabla T$. In other words, crossed gradients in electron number density and fluid temperature extract magnetic field energy from internal energy of the fluid.

The energy equation for a nonrelativistic conducting, viscous fluid may be written as:

$$\rho \frac{d\varepsilon}{dt} = \vec{J} \cdot \vec{E} - (pg^{ij} - \sigma^{ij}) \nabla_i v_j + \nabla \cdot (\kappa \nabla T) - v_i \nabla_j \left(B^i B^j - \frac{1}{2} g^{ij} B^2\right) \tag{46}$$

where ε is the specific internal energy, σ^{ij} the viscous stress dyad, and κ the thermal conductivity of the fluid. Inserting the electric field, $\vec{E}$, from Equation (45) into the above yields:

$$\rho \frac{d\varepsilon}{dt} = \frac{1}{\sigma} J^2 - (pg^{ij} - \sigma^{ij}) \nabla_i v_j + \nabla \cdot (\kappa \nabla T) - \frac{1}{e(1+\zeta)n_i} \vec{J} \cdot \nabla P \tag{47}$$

The last term in Equation (47) is the source of energy for thermally generated magnetic fields.

SECTION 5

THE THERMAL GENERATION OF MAGNETIC FIELDS

5.1 INTRODUCTION.

Recent experiments performed at NRL with the Pharos II and the Pharos III design involved the illuminating of thin planar targets by hundred-Joule laser pulses with intensities between 10^{12} and 10^{14} Watt/cm^2 that endure for a few nanoseconds. The computer code MACH2 (Peterkin, et al., 1986, Ref. 7), designed to perform two-dimensional simulations of plasmas in complex geometries, was used to simulate some of the NRL experiments that took place in environments of Nitrogen gas at pressures of a few Torr. In a previous report (Stellingwerf, Peterkin, Longmire, 1986, Ref. 8), we presented results of simulations of the laser-target-ambient system with MACH2 that illustrated the time development of the bubble that emanates from the laser-irradiated target and the laser-induced cylindrical expansion that leads to the formation of the aneurysm. In this section, we investigate the formation and development of magnetic fields that are generated from thermal energy near the laser focal spot.

5.2 LASER AND TARGET PARAMETERS.

The purpose of our investigation is two-fold. First, we wish to learn the magnitude as well as the spatial and temporal development of laser-induced magnetic fields. Second, we wish to learn what effect these fields may have on the dynamics of the laser-target-ambient system. To accomplish this, we performed two simulations from the same set of initial conditions. In the first, we do not model thermally-generated magnetic fields and in the second, we do. We then compare the state of the two simulations at identical times to learn what effect, if any, the thermally-generated magnetic fields have on the dynamics of the system.

Laser and target parameters used for the MACH2 simulations discussed herein are similar to those of a particular experiment performed at NRL in late 1985 (shot 85-544). The computational mesh used for the present sequence of MACH2 calculations is illustrated in Figure 25. The vertical line at the left of this figure is an axis of symmetry; rotation about this line is assumed. The target, located at the bottom of the mesh, is 100 μm thick, initially of density 2.7 gm/cc and at room temperature (0.025 eV). The ambient nitrogen pressure is 5 Torr and extends 5 mm from the target surface. For this investigation, we are interested in early-time development (the first 15 ns). To obtain sufficient resolution with a modest number of computational cells, we restrict our attention to the region close to the target surface. The laser spot is a circle of diameter 100 μm. The laser beam, centered on the axis of symmetry, propagates from the top of the mesh to the critical surface--that is the target surface at early times. The full opening angle of the converging laser beam is 5.92 degrees. The computational mesh is 36 × 36 cells with four cells across the beam and 4 cells across the thickness of the target. The boundaries of the computational region allow flow of material through them, and are electrically non-conducting.

The target in shot 85-544 was made from aluminium, and the ambient gas was nitrogen at an initial pressure of 5 Torr at room temperature. The target was a flat aluminium disk with a radius of 750 μm and a thickness of 5.6 μm. The thickness should have little effect on the blowoff emanating from the laser side of the target, so to avoid an unnecessarily small time-step, we model a 100 μm thick target in the simulation of this shot.

In these simulations, a pulse of 1.054 μm wavelength laser light, with an essentially Gaussian temporal shape, illuminates the target for 8.168 ns. The peak power occurs at 4.084 ns, and the full width at half maximum is 6.0 ns. Peak power is $2.29\ 10^{10}$ Watt, and a total of 109 J of energy is delivered to the target. The peak intensity is $6\ 10^{13}$ Watt/cm^2. The laser is focused onto a 100 μm radius circle on the target. All of the energy that is not absorbed by the ambient gas in the laser channel is

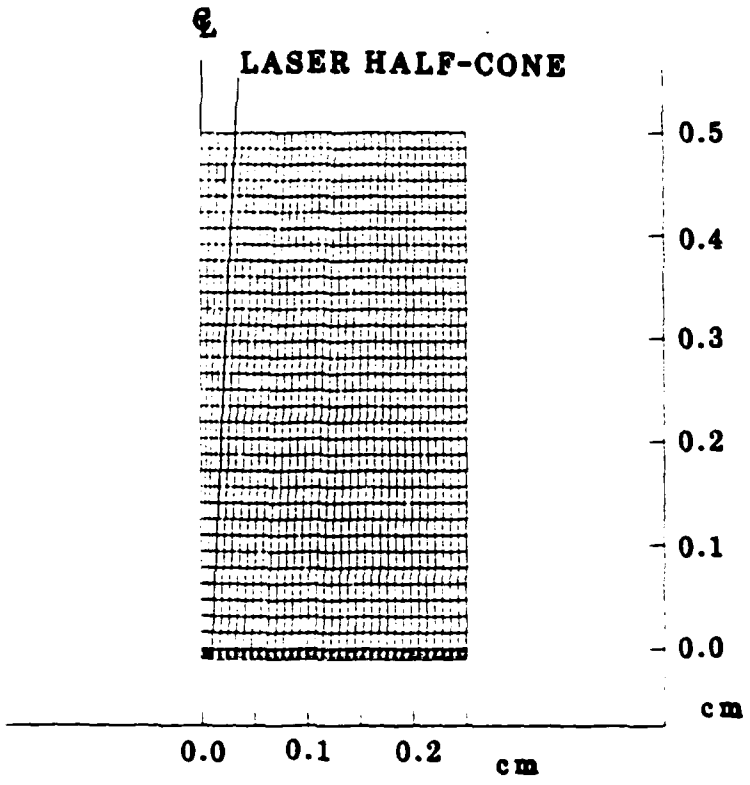

Figure 25. MACH2 calculation mesh for models sgmf2 and sgmf4.

absorbed at the critical surface (the surface in three-dimensional space at which the laser light first encounters material with density above the critical density--3.435 10^{-3} gm/cc for aluminium and 1.054 μm light). Laser light is assumed to be absorbed via inverse bremsstrahlung. The cold ambient gas is preionized in our models, presumably by X-rays from the target induced by the laser precursor. Our preionization model falls as $1/r^2$ from the target surface with five percent of the ambient atoms singly ionized 1 cm from the target. The preionization does not affect the temperature of the ambient gas.

Thermally-generated magnetic field arise from a curl of the pressure gradient divided by the sum of the electron and the ion number densities. Because these lie in the computational plane of MACH2, the curl is orthogonal to that plane and the resulting magnetic field is in the azimuthal direction.

5.3 SIMULATION RESULTS.

The diagrams in Figure 26 illustrate the first simulation (without a model of thermally-generated fields) 10 ns after the laser pulse began. The pictures of electron number density and temperature clearly show the cylindrical expansion from the laser heated channel. As the temperature in the channel rises, the density there falls below its ambient value in order to maintain approximate pressure equilibrium. The picture of velocity vectors shows a jet of material propagating up the low-density channel ahead of the expanding bubble outside the channel. (It is worth noting that simulations without laser heating of the channel show no such perturbation of the otherwise spherical bubble that emanates from the laser-heated target.)

The diagrams in Figure 27 illustrate the second simulation (with a model of thermally-generated fields) 10 ns after the laser pulse began. As with the first simulation, the pictures of electron number density and temperature clearly show the cylindrical expansion from the laser heated

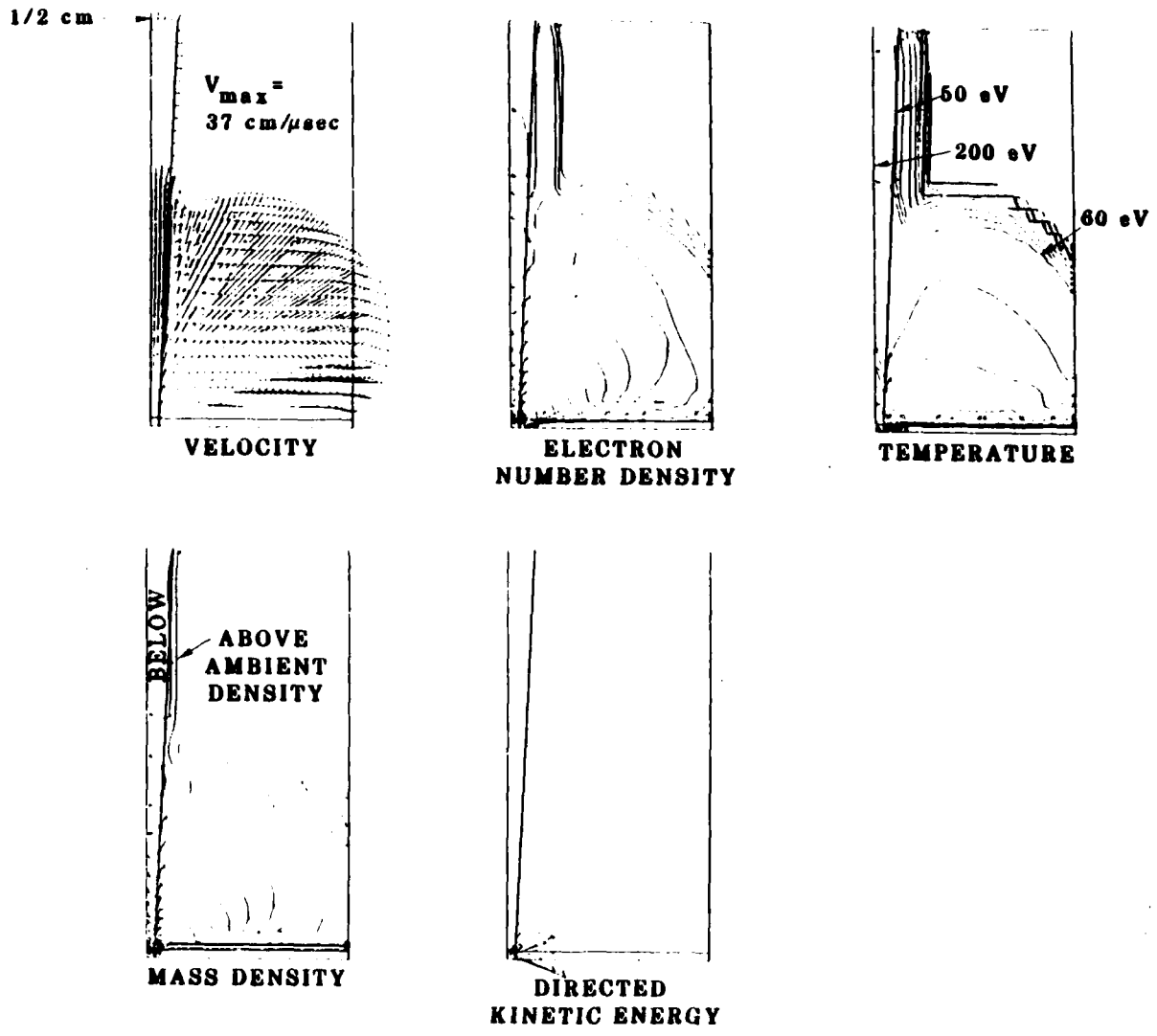

Figure 26. MACH2 model sgmf2 and 10 ns without a model of thermally-generated magnetic fields.

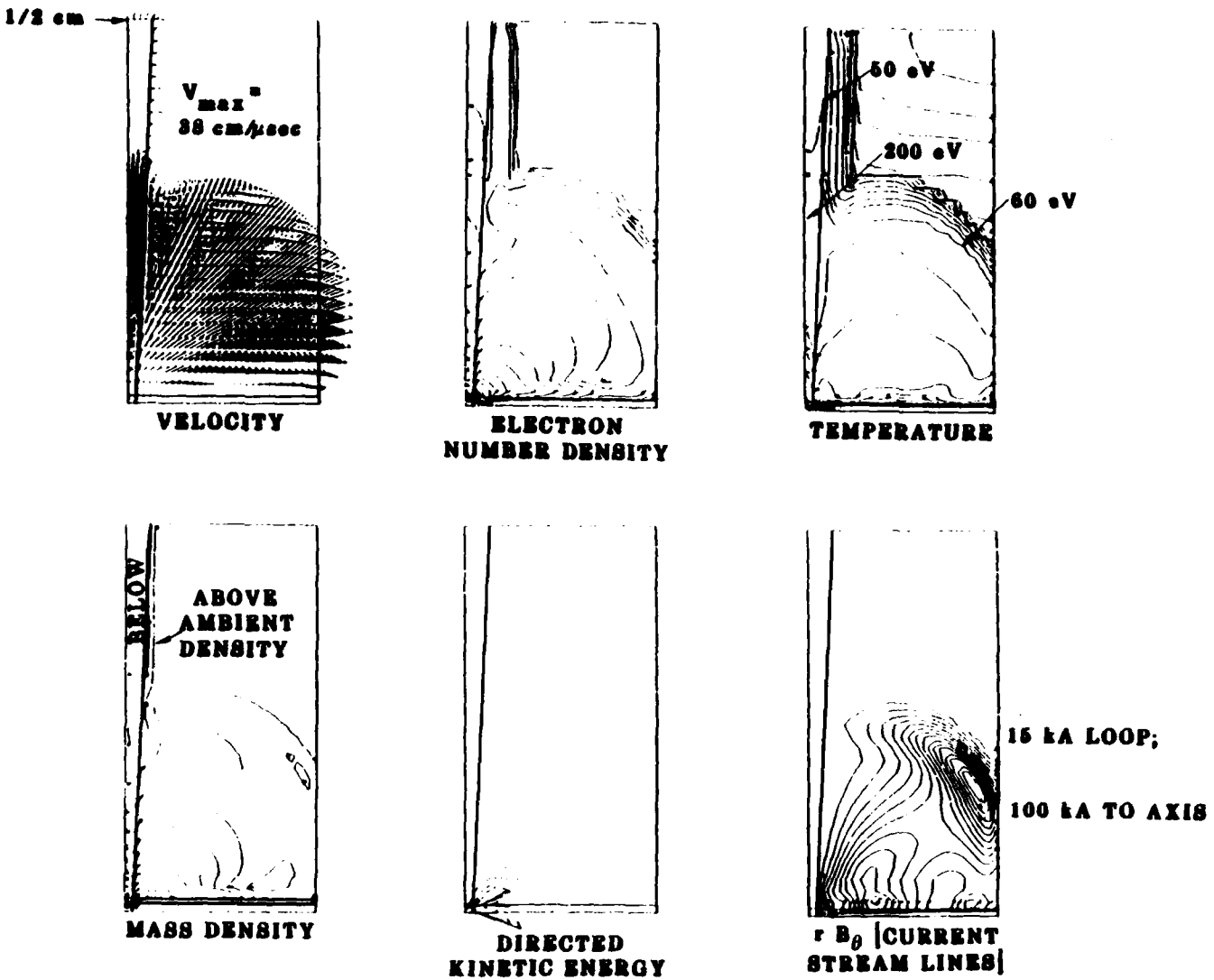

Figure 27. MACH2 model sgmf4 at 10 ns with a model of thermally-generated magnetic fields.

channel. In addition, a contour plot of rB (essentially current streamlines) is shown in Figure 27. Toroidal regions of field, with a peak value of 37 kG, appear concentrated directly behind the bubble. This toroidal region is oriented approximately 60 degrees from the laser axis. Poloidal current loops, with a peak current of 15 kA, circulate about the toroidal field lines. At this time 100 kA is flowing in the region between the axis and a location 2 mm from the axis. At 5 ns, immediately after the time of peak laser power, the magnetic induction reaches a maximum of nearly 1 MG in a limited region (one computational cell) near the laser focal spot. At this time, 100 kG fields envelope an extended region (a few computational cells) centered about the focal spot.

Despite the size of the current and magnetic field at early times, the state of the simulation at 10 ns is essentially unaffected by the thermal generation of magnetic fields. This leads us to conclude that, although rather strong fields are generated, they are a small perturbation and do not change the dynamics of the laser-target interaction by a noticeable amount. Although multi-kilogauss fields are generated, the fraction of laser energy that is converted to magnetic energy peaks at less than one percent as can be seen in Figure 28 if one recalls that the laser energy is 109 J.

Note also from Figure 28 that the magnetic energy peaks at the end of the laser pulse (8.2 ns). After this time the magnetic energy, which arose from plasma thermal energy in the first place, returns to plasma energy by the Joule heating mechanism. We conclude from this that the magnetic field is generated not by dynamics in the expanding bubble, but rather by the laser interacting with plasma near the critical surface. The non-zero size of the laser spot and the extent of the target create two-dimensional effects that are important to the early-time evolution of the expanding plasma and that create the crossed gradients of temperature and density that give rise to magnetic fields.

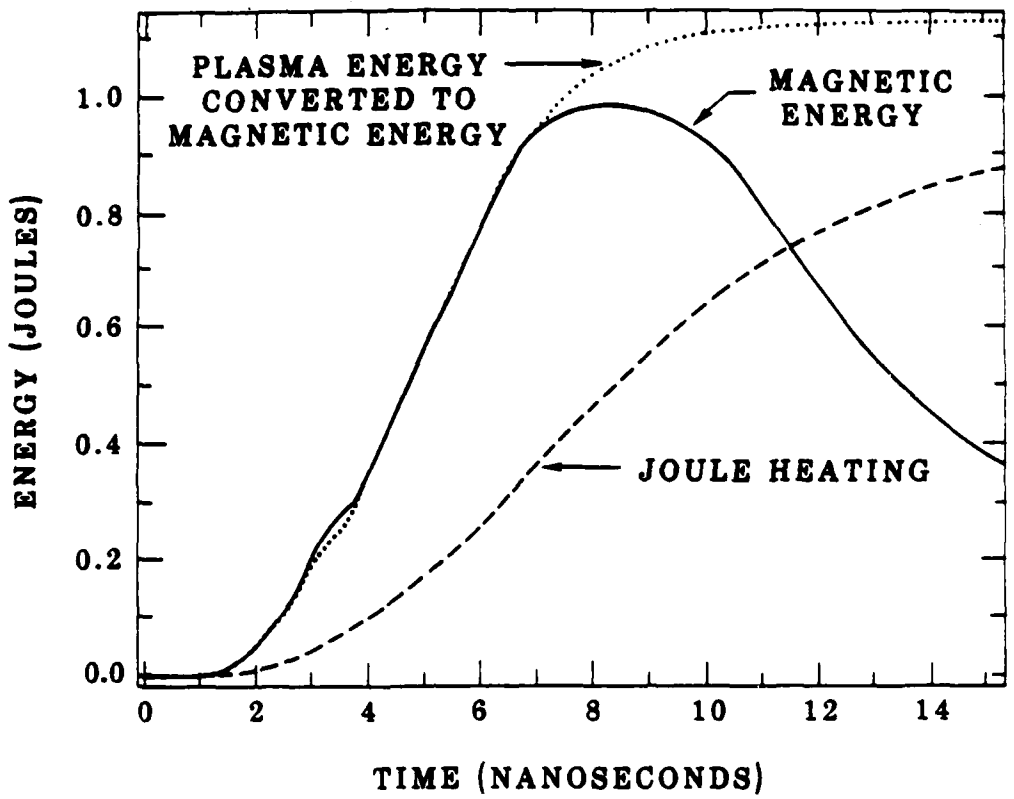

Figure 28. Magnetic energy versus time for MACH2 model sgmf4.

The expanding bubble is hot (tens of eV) and has a relatively high electrical conductivity. The magnetic field is therefore transported with the expanding plasma so field tends to reside within the bubble. This view is supported by Figure 29 where we show the state of the problem at 1 ns intervals for the first 10 ns of the second simulation. The plasma is not diffusive and the magnetic field is essentially trapped within the bubble.

Our model for thermal conduction is isotropic. However, it is well known that thermal conduction in a direction orthogonal to a strong magnetic field ($\omega_e \tau_e >> 1$) is suppressed because of the small gyroradius of the electron. Figures 30 and 31 illustrate the same simulation at 10 ns, but now with the anisotropic effects included (model sgmf10). The overall plasma configuration is very similar to that seen in Figure 27. The only significant difference between the two runs is a strong suppression of the thermal flux from the heated expanding shell in sgmf10, except in the heated channel. This has some effect on the temperature distribution in the shell and in the channel, but has little effect on the dynamics of the expanding shell and the aneurysm.

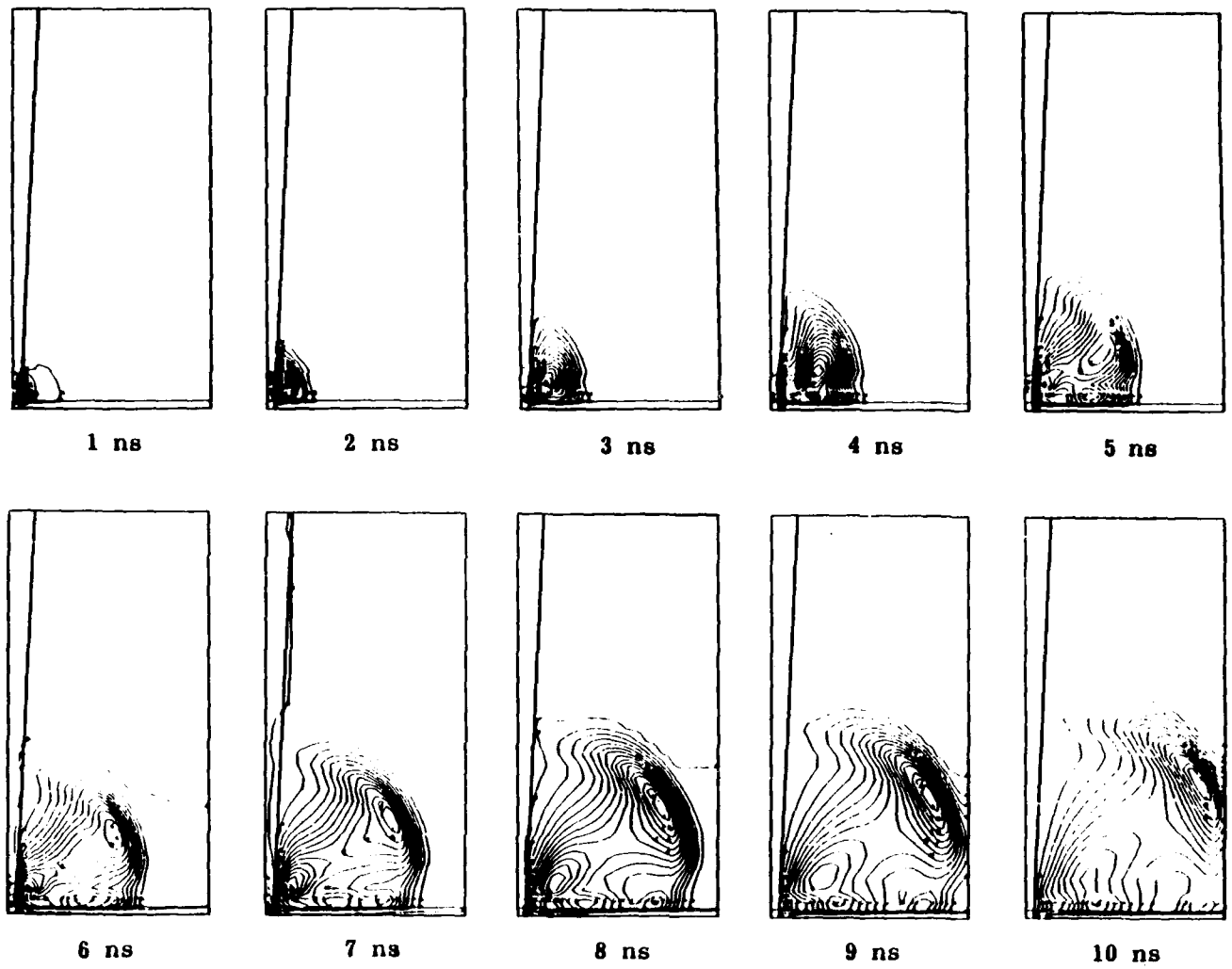

Figure 29 rB_θ plots at 1 ns intervals during laser pulse from MACH2 simulation sgmf4.

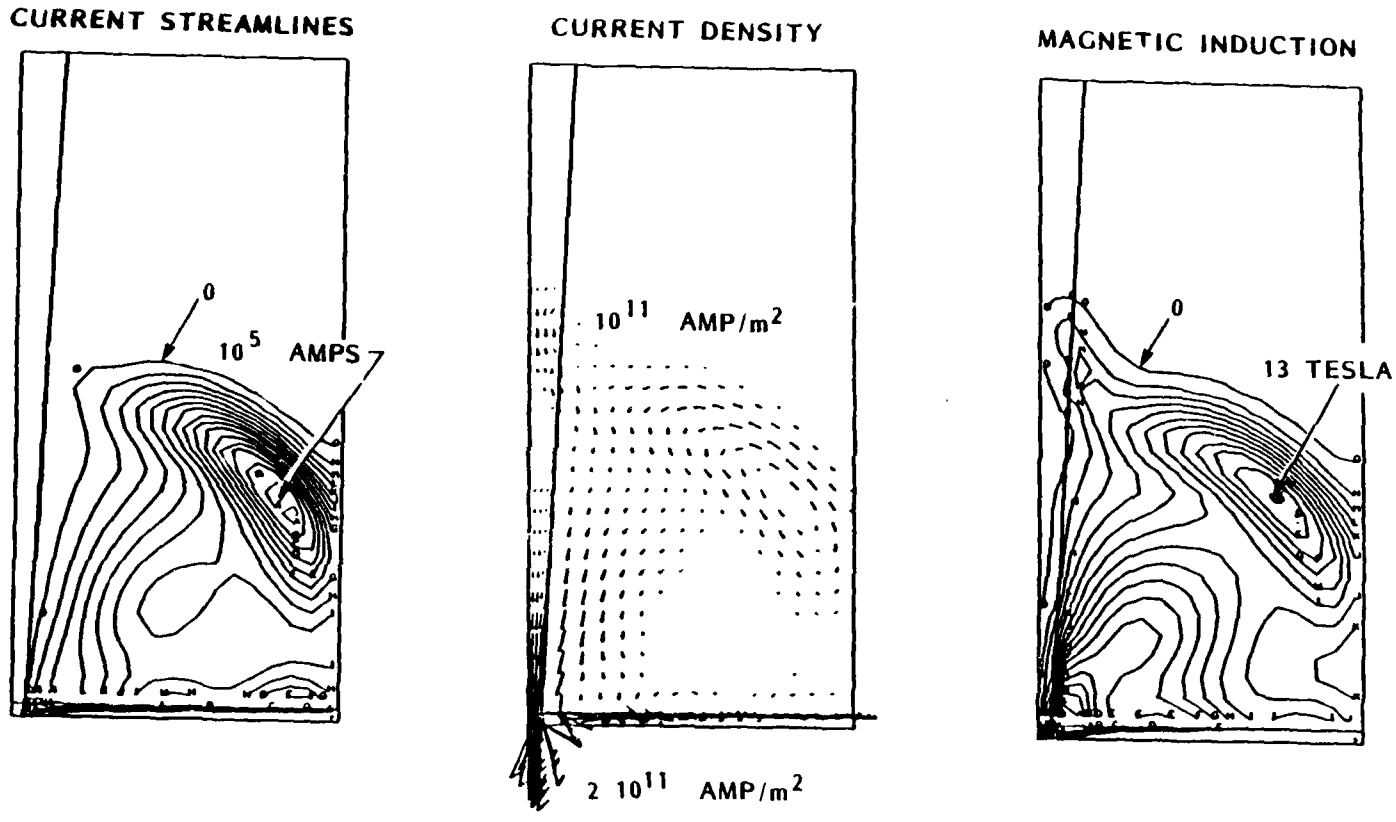

Figure 30. Current and magnetic field strength at 10 ns for the model sgmf10, including the effects of anisotropic magnetic fields.

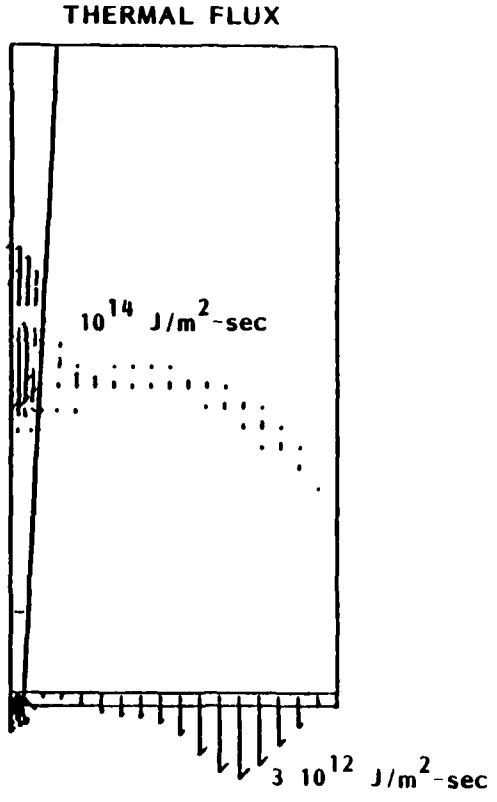

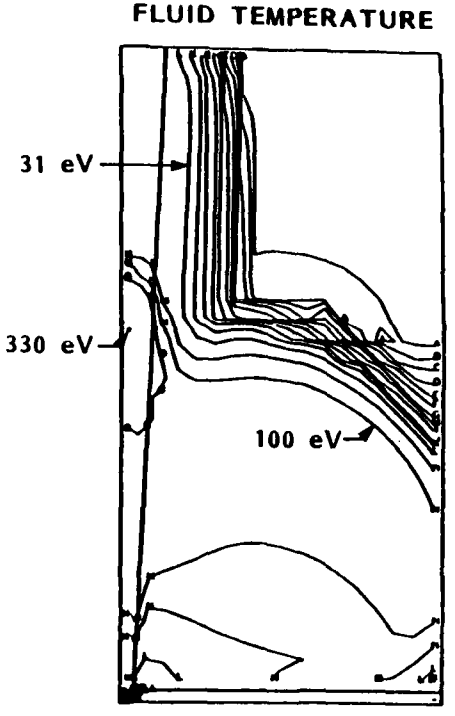

Figure 31. Thermal flux and temperature at 10 ns for the model sqmf10, including the effects of anisotropic magnetic fields.

SECTION 6

MAGNETIC BUBBLE FORMATION IN EXPANDING LASER PLASMA

As discussed in previous sections, the 2 1/2 D MHD code MACH2 has the capability of modeling an expanding plasma in the presence of a complex magnetic field configuration. Large toroidal fields generated by thermal gradients have been discussed in Sections 4 and 5. It is of interest to inquire whether such fields will interact with an ambient magnetic field, and what the evolution of the ambient field would be in such a case. In this section we present the results of initial tests of a laser/target simulation with a 10 kG ambient magnetic field, a value accessible to the NRL experimental setup. This run is designated "laser29".

The geometry of the simulation is shown in Figure 32. The parameters for this test computation are listed in Table 3.

Table 3. Laser29 parameters.

Laser Energy	110	J
Ambient Pressure	5	Torr
Pulse FWHM	6	ns
Spot Size	200	microns
Ambient Field	10	kG
Grid Height	0.5	cm
Grid Width	0.25	cm

The field configuration used here is unusual: the ambient field is parallel to the laser beam. This configuration has been chosen to preserve the cylindrical symmetry assumed in the simulation, and is a possible experimental configuration. Although the bulk of the plasma motion is along the field lines in this case, there remains a substantial cross-field motion as the spherical blast wave expands. In addition, this case allows a study of the behavior of the field near the plasma/(conducting) target interface.

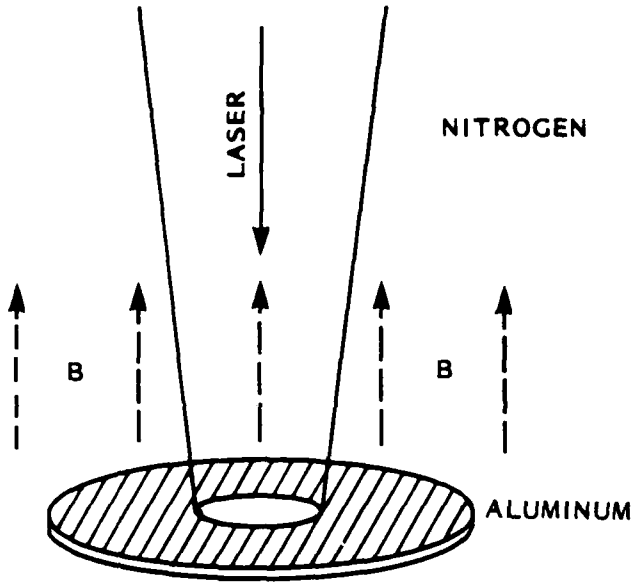

Figure 32. Geometry used in the ambient B-field simulation. Parameters are given in Table 3.

The results of this run are shown in Figures 33 through 37. The overall plasma configuration and plot diagnostics are very similar to the models discussed in previous sections, and detailed descriptions will not be repeated here. Each of these figures shows the situation at 5 ns, just following the peak of the laser pulse (at 4 ns), and also at 10 ns, just after the laser intensity drops to zero (at 8 ns).

We note from Figures 33 through 37 that the development of the shell and aneurysm is unaffected by the ambient field in this case. A comparison with the models in Section 5 indicates that the evolution of the self-generated magnetic field is also unaffected by the ambient field. The configuration of the field itself, shown in Figure 36, shows the field lines swept aside by the expanding plasma, while maintaining their connection at the target. The enhanced field at the axis near the target is an error, and does not occur in problems that are run with the most recent version of MACH2. The magnitude of the ambient field is not greatly changed by the motion of the plasma, and remains small compared with the size of the self-generated fields within the cavity.

This test computation is intended to be a test of the code for this type of problem, and to give some hint of what to expect. In a future report we will discuss the physics of the expanding magnetic cavity, and present a full series of models of various cases.

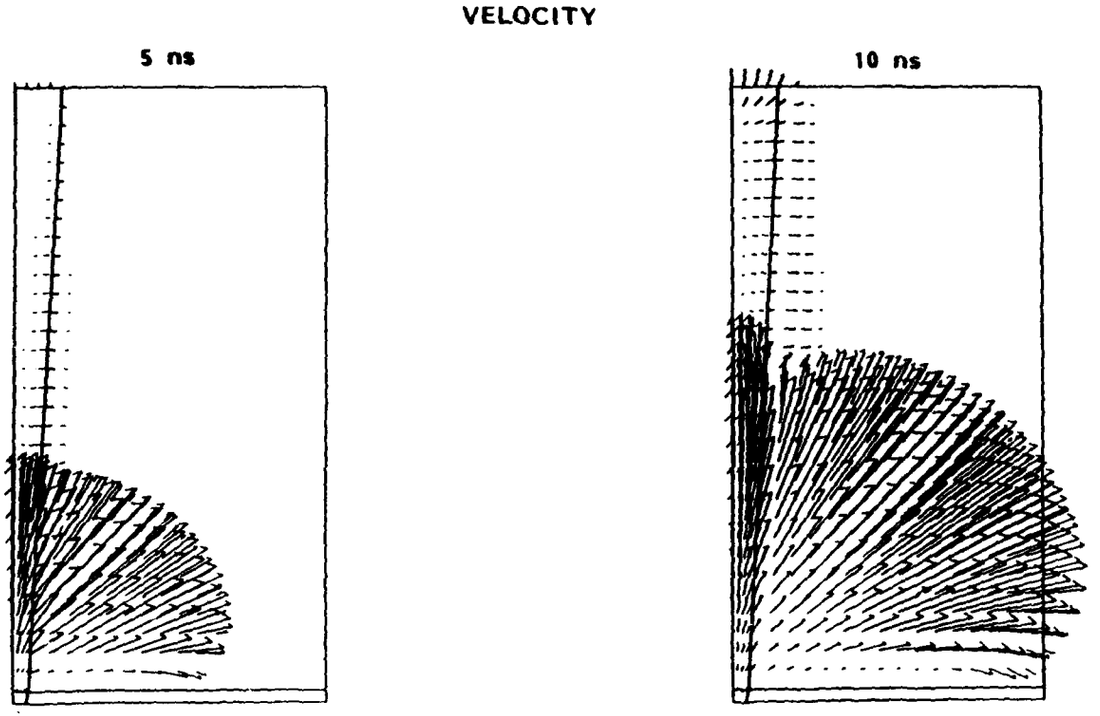

Figure 33. Velocity vector plots for the run "laser29" at 5 and 10 ns. Maximum velocities at the two times are 370 km/s and 270 km/s.

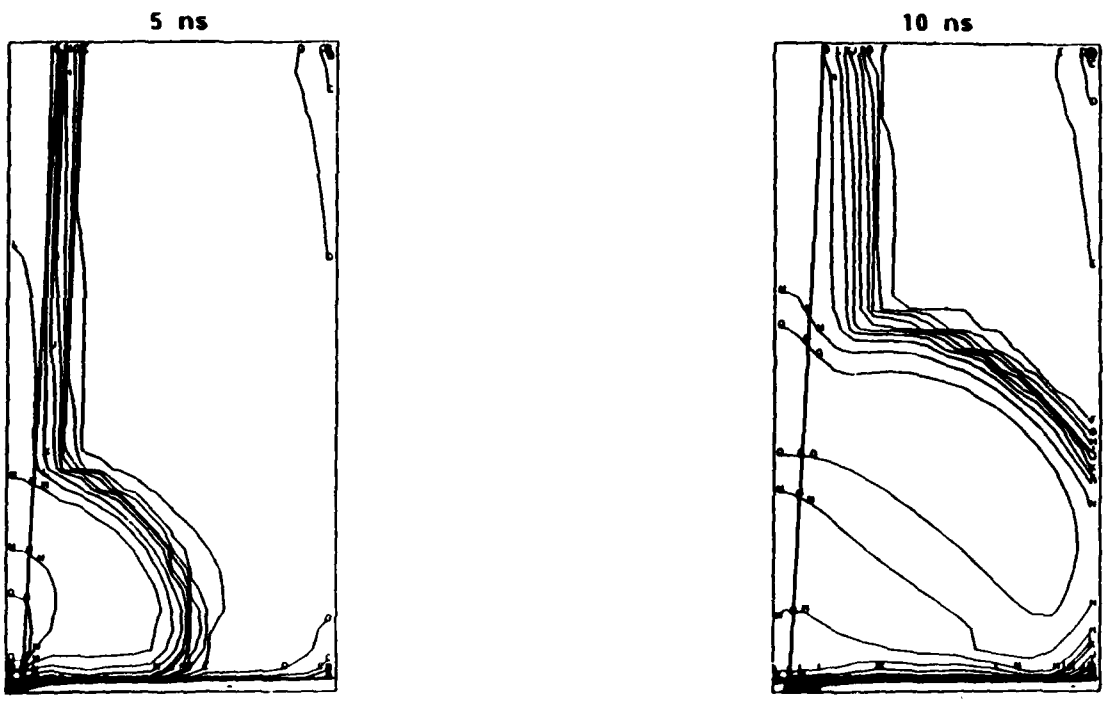

Figure 34. Temperature contour plots for the run "laser29" at 5 and 10 ns. The channel temperatures at the two times are 74 eV and 47 eV.

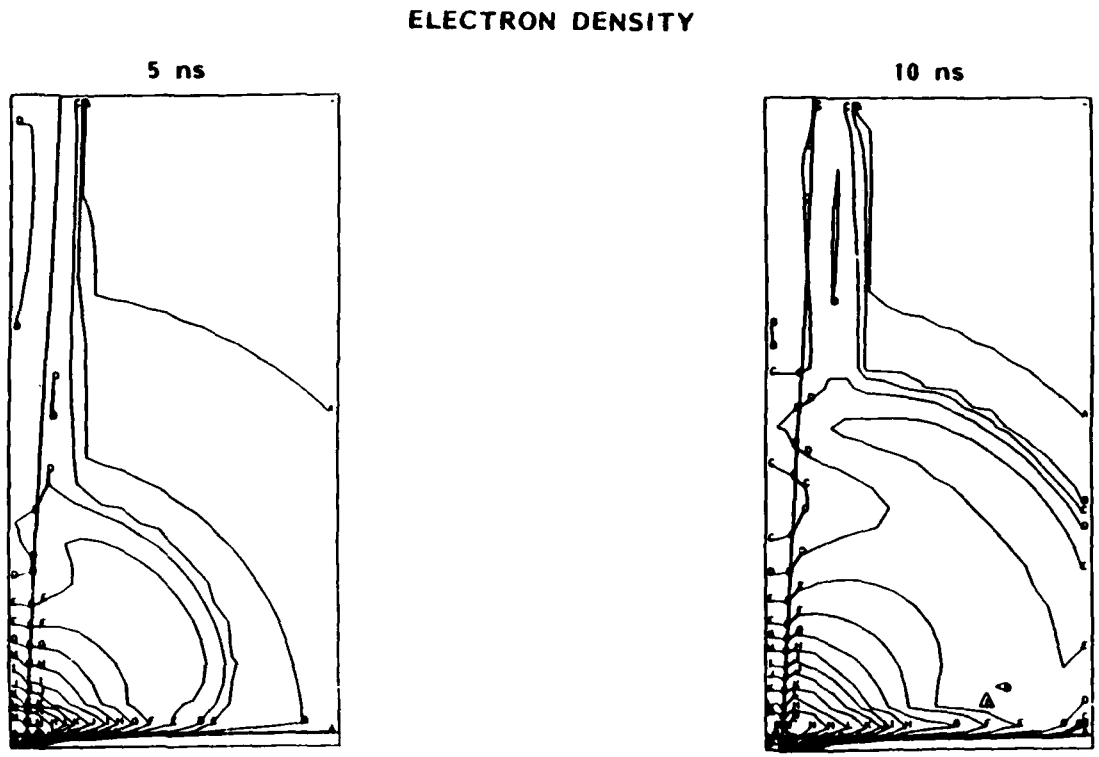

Figure 35. Electron density contour plots for the run "laser29" at 5 and 10 ns. Channel densities at the two times are 2.1e18 and 3.4e17.

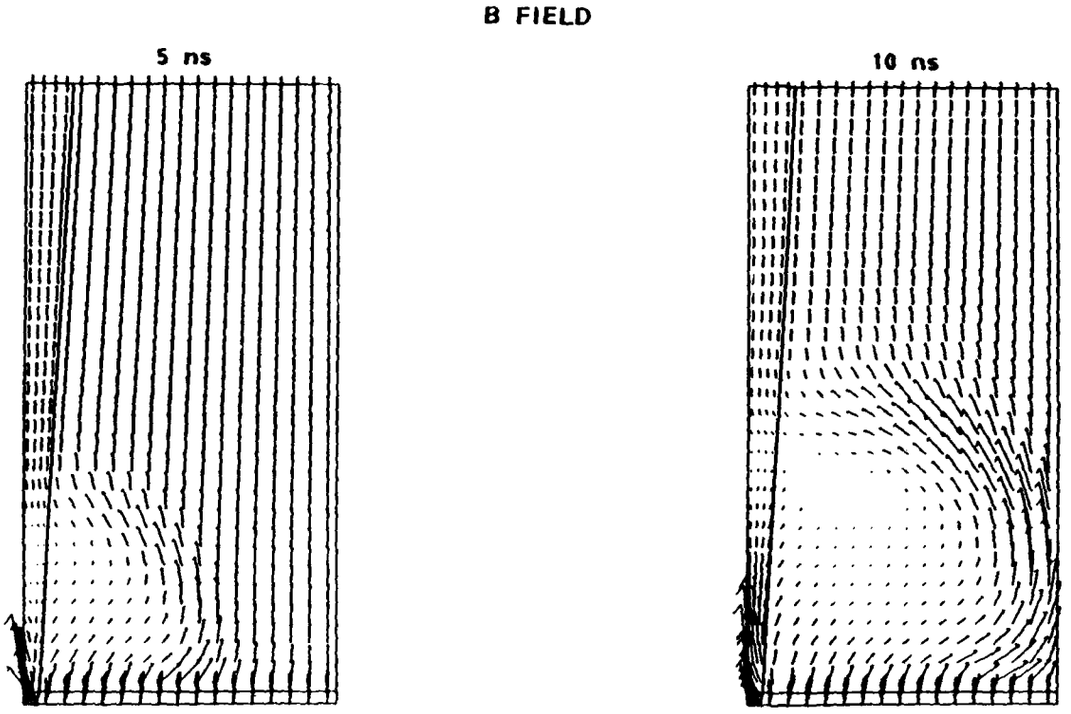

Figure 36. Magnetic field vector plots for the run "laser29" at 5 and 10 ns. Maximum values at the two times are 36 kG and 40 kG.

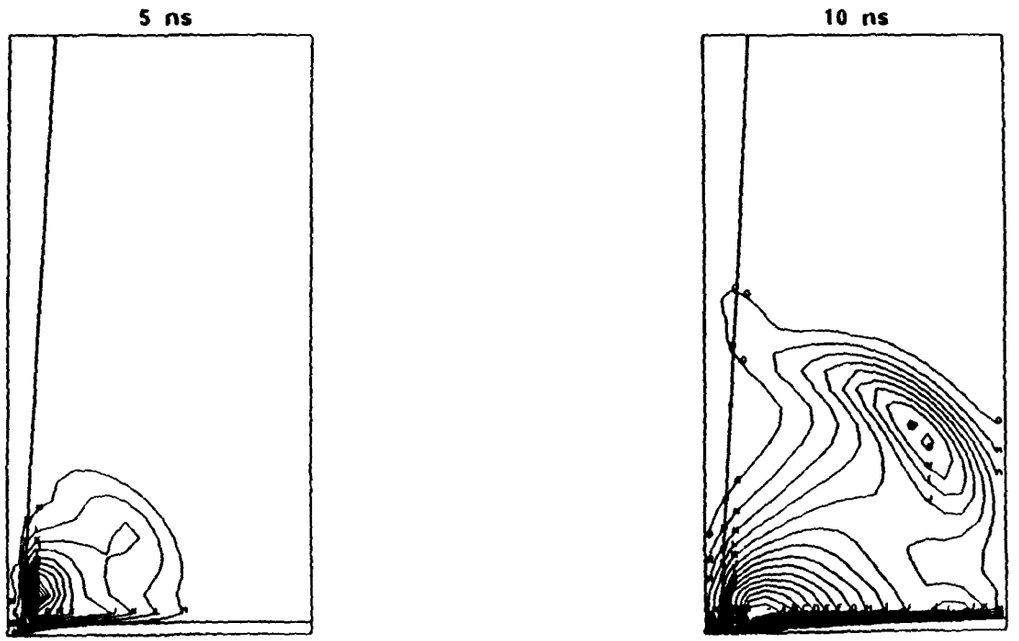

Figure 37. Toroidal magnetic field contour plots for the run "laser29" at 5 and 10 ns. Maximum values at the two times are 470 kG and 110 kG.

SECTION 7

LIST OF REFERENCES

1. J. Grun, R. F. Stellingwerf, and B. H. Ripin, Phys. Fluids 29, 10 (1986) (U).

2. B. H. Ripin, A. W. Ali, H. Griem, J. Grun, S. Kacenjar, C. K. Manka, E. A. McLean, A. M. Mostovych, S. P. Obenschain, and J. A. Stamper, in Laser Interaction and Related Plasma Phenomena, Vol. 7, edited by H. Hora and G. H. Miley (Plenum, New York, 1986) (U).

3. R. F. Stellingwerf, "NRL/HANE Laser Scrapbook 1983 - 1986," AMRC-R-858, 1987 (U).

4. J. A. Stamper, E. A. McLean, S. P. Obenschain, and B. H. Ripin, in Fast Electrical and Optical Measurements, Vol. II - Optical Measurements, edited by J. E. Thompson and L. H. Luessen (Martinus Nijhoff, Dordrecht, Netherlands, 1986) (U).

5. B. H. Ripin, J. A. Stamper, and E. A. McLean, "Blast-Wave Analysis of High Pressure Coupling Shells," NRL Memorandum Report 5279 (1984) (U).

6. M. H. Frese, "MACH2: A Two-Dimensional Magnetohydrodynamic Simulation Code for Complex Experimental Configurations, AMRC-R-874, September 1987 (U).

7. R. E. Peterkin, Jr., J. Buff, M. H. Frese, and A. J. Giancola, "MACH2: A Reference Manual - Second Edition," AMRC-R-851, 1986 (U).

8. R. F. Stellingwerf, R. E. Peterkin, Jr., and C. L. Longmire, "Studies of LASER-HANE Structure in Expanding Laser Plasma," AMRC-R-829, 1986 (U).

9. R. H. Lehmberg and S. P. Obenschain, Opt. Commun. 46, 27 (1983) (U).

10. R. E. Peterkin, Jr. and R. F. Stellingwerf, "Two-Dimensional Simulations of Laser-Target Interactions with MACH2: The Thermal Generation of Magnetic Fields," AMRC-N-365, 1987 (U).

11. J. L. Guillani, Jr., "Thermal Evaporation in Blast Waves: A Model for Aneurysm Formation in the NRL-LASER-HANE Simulation Experiment," NRL Memorandum Report 5492 (1985) (U).

12. J. G. Lyon, "Two-Dimension Simulations of the NRL Laser Experiment," NRL Memorandum 5491, (1985) (U).

13. E. M. Jones, J. Childers, and J. W. Kodis, "Geometry of Fireball Spikes: Priscilla and Socorro," Los Alamos Report, LA-10900-MS, (1987) (U).

14. T. W. Johnston and J. M. Dawson, Phys. Fluids 15, 5 (1973) (U).

15. Y. B. Zel'dovich and Y. P. Raizer, Physics of Shock Waves and High-Temperature Hydrodynamic Phenomena (Academic Press, New York, 1966) (U).

16. A. Brandt, "Multi-Level Adaptive Solutions to Boundary-Value Problems," Mathematics of Computation, 31, 138, pp. 333-390 (1977) (U).

17. T. W. Johnston and J. M. Dawson, Phys. Fluids 16, 722, (1973) (U).

18. L. Spitzer, Jr., Physics of Fully Ionized Gases, (New York, Interscience), 1962 (U).

DISTRIBUTION LIST

TR-88-112

DEPARTMENT OF DEFENSE

DEFENSE INTELLIGENCE AGENCY
2 CYS ATTN: RTS-2B

DEFENSE NUCLEAR AGENCY
ATTN: G ULLRICH
ATTN: NANF
ATTN: NASF
ATTN: OPNA
3 CYS ATTN: RAAE
ATTN: K SCHWARTZ
ATTN: L SCHROCK
ATTN: RAEE
4 CYS ATTN: TITL

DEFENSE TECHNICAL INFO CENTER
2 CYS ATTN: DTIC/FDAB

DEPARTMENT OF THE NAVY

NAVAL RESEARCH LABORATORY
ATTN: J GOODMAN
ATTN: S OSSAKOW
ATTN: J DAVIS
ATTN: B RIPIN
ATTN: P RODRIGUEZ
ATTN: J HUBA

DEPARTMENT OF THE AIR FORCE

AIR FORCE WEAPONS LABORATORY
ATTN: NTN
ATTN: SUL

DEPARTMENT OF ENERGY

LOS ALAMOS NATIONAL LABORATORY
ATTN: D SAPPENFIELD
ATTN: D SIMONS
ATTN: D WINSKE
ATTN: J WOLCOTT
ATTN: J ZINN
ATTN: R JEFFRIES
ATTN: R W WHITAKER
ATTN: T KUNKLE

DEPARTMENT OF DEFENSE CONTRACTORS

AUSTIN RESEARCH ASSOCIATES
ATTN: J THOMPSON

BERKELEY RSCH ASSOCIATES, INC
ATTN: C PRETTIE
ATTN: J WORKMAN
ATTN: S BRECHT

JAYCOR
ATTN: J SPERLING

KAMAN SCIENCES CORPORATION
ATTN: DASIAC

KAMAN TEMPO
ATTN: B GAMBILL
ATTN: DASIAC
ATTN: R RUTHERFORD
ATTN: W MCNAMARA

LOCKHEED MISSILES & SPACE CO, INC
ATTN: J HENLEY
ATTN: J KUMER
ATTN: R SEARS

MISSION RESEARCH CORP
ATTN: B R MILNER
ATTN: C LAUER
ATTN: D ARCHER
ATTN: D KNEPP
ATTN: F FAJEN
ATTN: F GUIGLIANO
ATTN: G MCCARTOR
ATTN: K COSNER
ATTN: M FIRESTONE
ATTN: R BIGONI
ATTN: R BOGUSCH
ATTN: R DANA
ATTN: R HENDRICK
ATTN: R KILB
ATTN: S GUTSCHE
ATTN: TECH LIBRARY

MISSION RESEARCH CORPORATION
2 CYS ATTN: R PETERKIN, JR.
2 CYS ATTN: R STALLINGWERF

NORTHWEST RESEARCH ASSOC, INC
ATTN: E FREMOUW

PACIFIC-SIERRA RESEARCH CORP
ATTN: E FIELD JR
ATTN: F THOMAS
ATTN: H BRODE

PHOTOMETRICS, INC
ATTN: I L KOFSKY

PHYSICAL RESEARCH INC
ATTN: W. SHIH

PHYSICAL RESEARCH INC
ATTN: H FITZ
ATTN: P LUNN

PHYSICAL RESEARCH, INC
ATTN: R DELIBERIS
ATTN: T STEPHENS

PHYSICAL RESEARCH, INC
ATTN: J DEVORE
ATTN: J THOMPSON
ATTN: W SCHLUETER

SCIENCE APPLICATIONS INTL CORP
ATTN: C SMITH
ATTN: D HAMLIN
ATTN: D SACHS
ATTN: E STRAKER
ATTN: L LINSON

SRI INTERNATIONAL
ATTN: D MCDANIEL
ATTN: W CHESNUT
ATTN: W JAYE

TOYON RESEARCH CORP
ATTN: J ISE

VISIDYNE, INC
ATTN: J CARPENTER